

# Sensitivity of the Stratospheric Climate and Age-of-Air to Finite-Volume Remapping Algorithm

Clara Orbe<sup>1,2</sup>, Lawrence L. Takacs<sup>3,4</sup>, Amal El Akkraoui<sup>3,4</sup>,  
Krzysztof Wargan<sup>3,4</sup>, Andrea Molod<sup>3</sup>, Steven Pawson<sup>3</sup>

<sup>1</sup>NASA Goddard Institute for Space Studies, New York, NY

<sup>2</sup>Department of Applied Physics and Applied Mathematics, Columbia University, New York, NY

<sup>3</sup>Global Modeling and Assimilation Office, NASA Goddard Space Flight Center, Greenbelt, MD

<sup>4</sup>Science Systems and Applications, Inc., Lanham, MD, USA

## Key Points:

- The stratospheric mean age-of-air simulated in GEOS is sensitive to the remapping scheme used within the finite-volume dynamical core.
- This sensitivity in the age-of-air is significant ( $\sim 30\%$ ) and imprints on the simulated distributions of several long-lived chemical trace gases, including nitrous oxide and methane.
- The age-of-air sensitivities primarily reflect changes in resolved wave convergence over the Northern Hemisphere midlatitude stratosphere, which impact mean upwelling in the tropical lower stratosphere.

---

Corresponding author: Clara Orbe, [clara.orbe@nasa.gov](mailto:clara.orbe@nasa.gov)

18 **Abstract**

19 Accurately modeling the large-scale transport of trace gases and aerosols is critical for interpreting past (and projecting future) changes in atmospheric composition. 20 Simulations of the stratospheric mean age-of-air continue to show persistent biases in chemistry climate models, although the drivers of these biases are not well understood. Here 21 we identify one driver of simulated stratospheric transport differences among various NASA 22 Global Earth Observing System (GEOS) candidate model versions under consideration 23 for the upcoming GEOS Retrospective analysis for the 21<sup>st</sup> Century (GEOS-R21C). In 24 particular, we show that the simulated age-of-air values are sensitive to the so-called “remap- 25 ping” algorithm used within the finite-volume dynamical core, which controls how in- 26 dividual material surfaces are vertically interpolated back to standard pressure levels af- 27 ter each horizontal advection time step. Differences in the age-of-air resulting from changes 28 within the remapping algorithm approach  $\sim 1$  year over the high latitude middle strato- 29 sphere – or about 30% climatological mean values – and imprint on several trace gases, 30 including methane ( $\text{CH}_4$ ) and nitrous oxide ( $\text{N}_2\text{O}$ ). These transport sensitivities reflect, 31 to first order, changes in the strength of tropical upwelling in the lower stratosphere (70- 32 100 hPa) which are driven by changes in resolved wave convergence over northern mid- 33 latitudes as (critical lines of) wave propagation shift in latitude. Our results strongly sup- 34 port continued examination of the role of numerics in contributing to transport biases 35 in composition modeling. 36 37

38 **Plain Language Summary**

39 Large-scale transport plays a crucial role in distributing climatically important trace 40 constituents in the atmosphere, especially in the stratosphere where transport largely 41 determines the chemical lifetimes of trace gases. One summary of transport in the strato- 42 sphere is the “mean age” or the mean transit time since air at a point in the stratosphere 43 was last in the troposphere. Current models used for simulating stratospheric compo- 44 sition produce a range of simulated ages, although these differences are poorly under- 45 stood. Among other factors, model numerics play a critical role in transport, but few 46 studies have explored the sensitivity of the mean age to the choice of numerical scheme 47 employed within different dynamical cores. Here we use one model to show that the mean 48 age is sensitive to the so-called “remapping” algorithm used within the finite-volume dy- 49 namical core that controls how individual material surfaces are vertically interpolated 50 back to standard pressure levels after each horizontal advection time step. This reflects 51 sensitivities in the representation of how waves propagate from the troposphere into the 52 stratosphere. This work suggests that model numerics can be an important factor in con- 53 tributing to differences in simulated transport among models.

54 **1 Introduction**

55 The chemical and radiative properties of the troposphere and lower stratosphere 56 are strongly influenced by the stratosphere-troposphere exchange of mass and tracers (e.g., 57 Morgenstern and Carver (2001); Hegglin et al. (2006); Pan et al. (2007)). Properly sim- 58 ulating the stratospheric circulation and its influence on atmospheric composition in earth 59 system models is important for capturing past decadal trends in surface climate, par- 60 ticularly in response to changes in Southern Hemisphere ozone depletion (e.g., Son et 61 al. (2009); Polvani et al. (2011)). In the Northern Hemisphere (NH), the stratospheric 62 circulation’s coupling to ozone could represent an important feedback on the climate’s 63 response to future increases in greenhouse gases (GHGs), especially over the North At- 64 lantic (e.g., Chiodo and Polvani (2019)). On shorter subseasonal timescales, stratospheric 65 ozone changes associated with strong polar vortex states may also modulate Arctic sea 66 level pressure and surface temperatures (e.g., Ivy et al. (2017); Oehrlein et al. (2020)), 67 so much so that seasonal forecast systems employing prognostic ozone show suggestions

68 of increased signal-to-noise ratio in predictions of the North Atlantic Oscillation (B. M. Monge-  
69 Sanz et al. (2022)).

70 Key to accurately simulating a consistent representation of coupling between strato-  
71 spheric dynamics and chemical trace gases is ensuring that a model’s underlying trans-  
72 port circulation is properly represented. To this end, much effort has been paid to de-  
73 veloping and refining so-called “tracer-independent” metrics of transport (Holzer and Hall  
74 (2000)) such as the mean age-of-air (Hall and Plumb (1994)) and to applying these mea-  
75 sures to rigorously evaluate model transport characteristics in chemistry climate mod-  
76 els (CCMs) (e.g., Hall et al. (1999); Orbe et al. (2018); Dietmüller et al. (2018); Aba-  
77 los et al. (2020)).

78 While the assessment of CCMs participating in the SPARC Chemistry Climate Model  
79 Validation (SPARC CCMVal) effort showed a marked improvement in simulated trans-  
80 port characteristics relative to previous intercomparisons (J. Neu et al. (2010)), more re-  
81 cent analysis of models participating in the SPARC Chemistry Climate Modeling Ini-  
82 tiative (CCMI) (Eyring et al. (2013)) do not demonstrate any improvement (Dietmüller  
83 et al. (2018), see their Figure 3). In particular, although some models produce mean age  
84 values that agree well with observational estimates, the CCMI intermodel spread is  $\sim$   
85 50%, with models generally simulating transport that is too vigorous relative to obser-  
86 vations. While documenting these transport differences among models is straightforward,  
87 understanding the drivers of this spread remains a key challenge and there is still no con-  
88 sensus on what is causing the large spread in simulated ages among the current gener-  
89 ation of CCMs.

90 A key challenge in identifying the drivers of age-of-air – and other stratospheric trans-  
91 port – biases is that they reflect the time-integrated effects of advection by the residual  
92 mean circulation and eddy diffusive mixing, or the quasi-random transport due to the  
93 breaking of Rossby waves (e.g., Holton et al. (1995); Plumb (2002)). Given that the in-  
94 fluences of mixing and advection are not easily separable, studies have come to differ-  
95 ent conclusions about sources of age biases in models. In particular, the analysis of the  
96 CCMVal models showed a strong correlation between the intermodel spread in the age-  
97 of-air and lower stratospheric tropical upwelling, whereas Dietmüller et al. (2018) showed  
98 that the age spread among the CCMI models was driven by differences in mixing. While  
99 future attempts to further distinguish between sources of age biases using either simpli-  
100 fied “leaky pipe” models (Plumb (1996); J. L. Neu and Plumb (1999)) or more complete  
101 measures of the transport circulation such as the “age spectrum” (e.g., Hall and Plumb  
102 (1994); Waugh and Hall (2002))) may prove enlightening, at present there is no consen-  
103 sus on what is causing large simulated age-of-air biases in models.

104 One potential limitation of previous work based on multi-model intercomparisons  
105 is that many aspects of model formulation can influence both stratospheric upwelling and  
106 mixing. Thus, while intercomparisons are useful for identifying common model biases,  
107 understanding the drivers of these biases is difficult absent single model-based process  
108 studies. Among these, several aspects of model formulation have been identified as in-  
109 fluencing simulated mean age distributions. As the mean age is sensitive to vertical mo-  
110 tion in the lowermost stratosphere, these include large sensitivities to vertical resolution  
111 (Orbe et al. (2020)) and to spurious vertical mixing either introduced in vertical coor-  
112 dinate transformations in offline chemical transport models (B. Monge-Sanz et al. (2007))  
113 or through use of assimilated winds performed either in offline (e.g., Legras et al. (2004))  
114 or online data assimilation and “nudged” configurations (e.g., Pawson et al. (2007); Orbe  
115 et al. (2017); Davis et al. (2022)). These age sensitivities can be still further amplified,  
116 depending on whether or not parameterized gravity waves are included (Eichinger et al.  
117 (2020)).

118 By comparison, sensitivities of the mean age to underlying tracer numerics have  
119 been less well examined, although Eluszkiewicz et al. (2000) documented a large sensi-

120 tivity in simulated age-of-air values to the choice of advection scheme. More recently,  
 121 Gupta et al. (2020) showed differences of  $\sim 25\%$  in the age-of-air across identical exper-  
 122 iments performed using four different dynamical cores, especially between those using  
 123 spectral versus finite-volume schemes. The experiments employed in that study, how-  
 124 ever, were highly idealized and it is not clear if the strong influence of tracer numerics  
 125 that they identified is also realized in more comprehensive model simulations with moist  
 126 physics, especially in the context of model development as carried out in operational mod-  
 127 eling centers.

128 To better elucidate this influence of tracer numerics on the transport properties sim-  
 129 ulated in a comprehensive global model context, here we document the sensitivity of the  
 130 stratospheric mean age in several recent versions of the NASA Global Earth Observing  
 131 System (GEOS) general circulation model (Molod et al., 2015). The versions examined  
 132 here represent different stages in model development since the Modern-Era Retrospec-  
 133 tive Analysis for Research and Applications Version 2 (MERRA-2; Gelaro et al. (2017)).

134 Our focus on transport evaluation is in wake of the upcoming release of the GEOS  
 135 Retrospective analysis for the early 21<sup>st</sup> Century (GEOS-R21C), which is an atmospheric  
 136 reanalysis that includes many advances over MERRA-2, and serves as a step towards  
 137 MERRA-3, a planned coupled Earth system reanalysis. As part of the current effort to  
 138 explore coupling of more Earth System components targeting MERRA-3, MERRA-21C  
 139 will be used to drive an off-line chemistry reanalysis R21C-Chem with a full chemistry  
 140 model (GEOS-Chem) and an advanced Constituent Data Assimilation component to up-  
 141 date the chemistry fields. Since R21C-Chem will be produced in replay-mode (one-way  
 142 coupling) whereby the meteorology fields are used to define the background atmospheric  
 143 flow (Orbe et al., 2017), it is imperative that GEOS-R21C produces a credible represen-  
 144 tation of transport processes.

145 In particular, here we document how in the process of evaluating candidate sys-  
 146 tems for GEOS-R21C we found that the mean age was  $\sim 1$  year younger (or  $\sim 30\%$  smaller)  
 147 than the values simulated in the model version used to produce MERRA-2 (Figure 1).  
 148 The model versions shown in Figure 1 reflect more than 10 years’ worth of accumulated  
 149 changes in model development, most notably changes in radiation, parameterized con-  
 150 vection and, as we focus on here, changes in the model’s description of vertical advec-  
 151 tion. More precisely, we show that slight modifications to the so-called “remapping” al-  
 152 gorithm, which is used to transform advected fields from Lagrangian levels to the new  
 153 pressure levels after each horizontal advection time step, are the primary driver of the  
 154 age-of-air changes exhibited in recent GEOS-R21C candidate model versions. Thus, whereas  
 155 Gupta et al. (2020) highlighted large differences between dynamical cores employing spec-  
 156 tral versus finite-volume (FV) numerics, our results show that large transport differences  
 157 can occur even within a given FV dynamical core, a result which may have broader im-  
 158 plications for other general circulation models employing FV numerics. We begin by dis-  
 159 cussing methods in Section 2 and present key results and conclusions in Sections 3 and  
 160 4, respectively.

## 161 2 Methods

### 162 2.1 Model Configurations

163 Here we present results from several versions of GEOS spanning MERRA-2 to more  
 164 recent candidates for GEOS-R21C. Among these model versions, a subset are more “of-  
 165 ficial” as they have been documented and/or employed in recent model intercomparisons  
 166 and are highlighted in Figure 1. In particular, these include a model version that was  
 167 used in Phase 1 of CCM1 and documented in Orbe et al. (2017) (Fig. 1, red line). A more  
 168 recent model version that was used in the CCM1 Phase 2 simulations (correspondence  
 169 with Michael Manyin) is also shown (Fig. 1, green line).

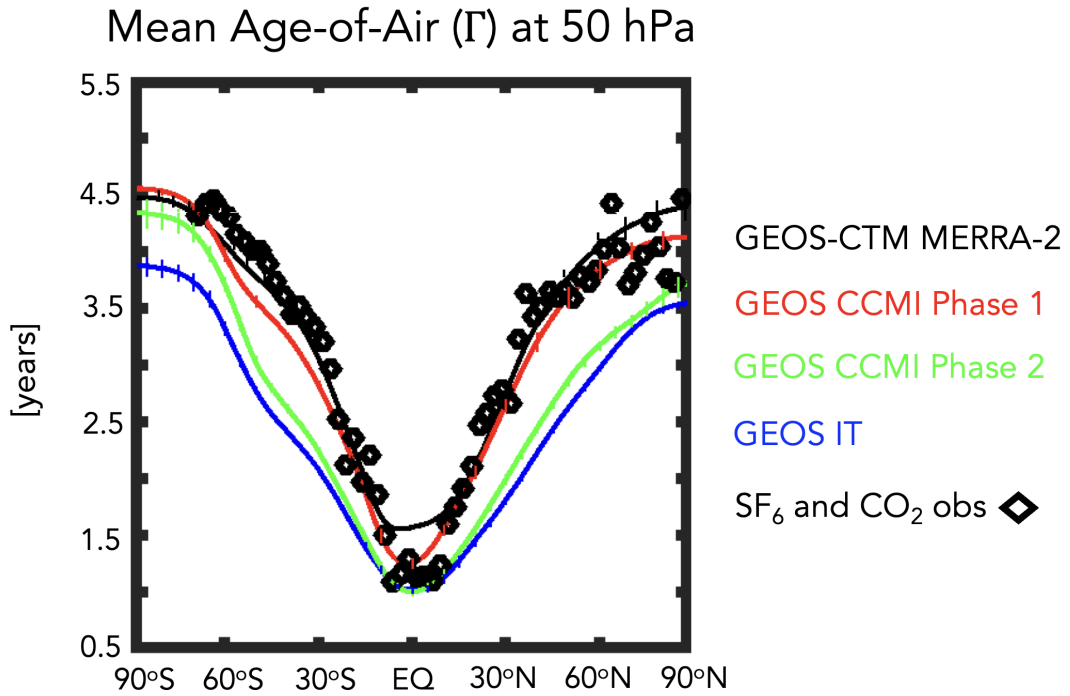


**Figure 1.** The 2000-2010 climatological annual mean meridional profile of the stratospheric mean age-of-air ( $\Gamma$ ), evaluated at 50 hPa. Results from a GEOS-CTM integration constrained with MERRA-2 meteorological fields (black line) as well as free-running GEOS simulations using a model configuration for CCM1 Phase 1 (red line), CCM1 Phase 2 (green line) and the GEOS-IT Version 5.29.4 dating from October 19, 2022 (hereafter simply "GEOS-IT", blue line) are shown. All simulations are constrained with the same (observed) historical sea surface temperatures. Diamonds correspond to SF<sub>6</sub> and CO<sub>2</sub> in situ based estimates of  $\Gamma$  from Boering et al. (1996) and Engel et al. (2009). Vertical dashed lines denote  $\pm\sigma$ , the standard deviation of  $\Gamma$  over 2000-2010, for each model simulation.

170 We begin by comparing 10-year (2000-2010) climatological mean zonally averaged  
 171 age-of-air profiles at 50 hPa across this subset of model versions, derived from 30-year  
 172 long atmosphere-only (AMIP) integrations constrained with observed sea surface tem-  
 173 peratures (Figure 1). First, we note that the profiles for the CCMI Phase 1 version of  
 174 the model are very close to observations (black stars), consistent with the  
 175 “GEOSCCM” documented age characteristics reported in Dietmüller et al. (2018) (see  
 176 their Figure 3). In addition, while passive tracers were not integrated within MERRA-  
 177 2, results using the GEOS chemistry transport model (GEOS-CTM, Kouatchou et al.  
 178 (2015)) constrained with MERRA-2 meteorological fields (black line) also exhibits good  
 179 agreement with observed values. This good agreement between the CTM-generated age-  
 180 of-air and the observations is consistent with results from a previous GEOS-CTM sim-  
 181 ulation (constrained with MERRA) as documented in Orbe et al. (2017).

182 Moving to more recent development versions of the model (green and blue lines),  
 183 however, reveals a reduction in the mean age by  $\sim 1$  year over both southern and north-  
 184 ern high extratropical latitudes, or a decrease of  $\sim 20$ -30% relative to the MERRA-2 con-  
 185 strained simulation and the observations. As discussed earlier, the green line refers to  
 186 the CCMI Phase 2 model version, whereas the blue line refers to the GEOS-IT Version  
 187 5.29.4 dating from October 19, 2022 (hereafter simply “GEOS-IT”). Note that this de-  
 188 crease in the climatological age in both model versions far exceeds the (internal) vari-  
 189 ations in mean age that occur interannually (vertical bars on solid lines).

190 Since MERRA-2, numerous updates have been introduced in to the GEOS model.  
 191 This includes replacing the Chou Suarez (Chou & Suarez, 1994) and Chou (Chou, 1990,  
 192 1992) radiation codes with the Rapid Radiative Transfer Model for GCMS (RRTMG;  
 193 Iacono et al. (2008), which impacts the stratosphere; the introduction of the Grell-Freitas  
 194 deep-convection code (Grell and Freitas (2014); Freitas et al. (2018)), which has a min-  
 195 imal impact on this study; and the upgrade from the GMAO FV core of Lin (2004) to  
 196 the GFDL FV3 dynamical core (Lin et al., 2017).

197 As we show in Section 3, the latter transition from the GMAO FV to the GFDL  
 198 FV3 core has the largest impact on the simulated age-of-air values. This degradation in  
 199 simulated transport within the GFDL FV3 core primarily reflects differences in the im-  
 200 plementation of the remapping algorithm, which is used to vertically interpolate indi-  
 201 vidual material surfaces after each horizontal advection step back to the model’s refer-  
 202 ence Eulerian coordinate. In its implementation in MERRA-2 within the GMAO FV core  
 203 (Table 1), this remapping involves 1) fitting piecewise parabolic (hereafter PPM) func-  
 204 tions to input layer-mean values of  $U$ ,  $V$ ,  $Q$  and tracers; 2) calculating PPM functions  
 205 to output layer edges; 3) integrating PPM functions between output layer edges to pro-  
 206 duce new layer-mean values of  $U$ ,  $V$ ,  $Q$  and tracers; 4) calculating total energy (TE) at  
 207 input mid-layer pressures; 5) calculating TE at output mid-layer pressures using cubic  
 208 interpolation and applying an a-posteriori integral conservation; and, finally, 6) remap-  
 209 ping temperatures from total energy via  $T = (TE - K - \Phi)/C_p$ . Here  $T$ ,  $U$ ,  $V$ ,  $Q$ ,  $C_p$ ,  
 210  $K$  and  $\Phi$  correspond to temperature, zonal wind, meridional wind, specific humidity, spe-  
 211 cific heat capacity and kinetic and potential energy, respectively.

212 When implemented within the GFDL FV3 core this remapping algorithm yields  
 213 degradations in simulated stratospheric transport. As the two dynamical cores are too  
 214 different to meaningfully compare in an apples-to-apples fashion, we use targeted exper-  
 215 iments with the GMAO FV core to show that the degradations in simulated transport  
 216 in the GFDL FV core resemble changes that occur when using a lower order (quadratic  
 217 vs. cubic) interpolation scheme in Step 5 of the remapping algorithm (Table 1). This  
 218 otherwise innocuous change in interpolation order in turn highlights the large sensitiv-  
 219 ities in transport that can occur even *within* a given finite-volume numerical scheme, in  
 220 our case resulting in large differences in lower stratospheric upwelling and a  $\sim 30\%$  re-  
 221 duction in the simulated mean age of air.

**Table 1. GMAO Core Finite-Volume Remapping Algorithm:** The remapping algorithm examined in this study controls how individual material surfaces are vertically interpolated back to standard pressure levels. Employing linear – and to a lesser extent – quadratic interpolation in Step 5 produces stratospheric transport characteristics that are more consistent with the most recent GEOS model configurations (green and blue lines, Figure 1), whereas a cubic interpolation is more consistent with older configurations (red and black lines, Figure 1) and with MERRA-2. Here  $T$ ,  $U$ ,  $V$ ,  $Q$ ,  $C_p$ ,  $K$  and  $\Phi$  correspond to temperature, zonal wind, meridional wind, specific humidity, specific heat of air at constant pressure and kinetic and potential energy, respectively.

Step	REMAP Procedure (MERRA-2, GMAO FV Core)
1	Fit PPM functions to input layer-mean $U$ , $V$ , $Q$ and tracers
2	Calculate PPM to output layer edges
3	Integrate PPM functions between output layer edges to produce new layer- mean $U$ , $V$ , $Q$ and tracers
4	Calculate $TE = C_p T + K + \Phi$ at input mid-layer pressures
5	Calculate $TE$ at output mid-layer pressures using cubic interpolation and a-posteriori integral conservation
6	Construct “remapped” $T$ via $T = (TE - K - \Phi)/C_p$

222

## 2.2 Model Experiments

223

### 2.2.1 AMIP vs. EMIP

224

225

226

227

228

229

230

We begin our analysis by interpreting the results shown in Figure 1, which are all based on historical AMIPs that were performed at the same cubed sphere C180 (approximately half-degree) horizontal resolution. As they represent more official model versions they serve as an important motivation for the experiments that follow. However, there are numerous (potentially compensating) development changes between these model versions which renders it nearly impossible to cleanly identify drivers of differences in their simulated transport.

231

232

233

234

235

To this end, in order to investigate the drivers of the differences in Figure 1 we perform targeted modeling experiments aimed at disentangling the influence of individual model development changes on stratospheric transport properties (Table 2). In order to evaluate impacts on transport climate statistics, we consider both a set of climatological AMIP (rows 1-4) as well as so-called “EMIP” (rows 5-7) experiments.

236

237

238

239

240

241

242

243

In particular, we carry out 30-year-long AMIP simulations at C180 resolution which we use to infer the climate characteristics of the different model configurations. The “EMIP” experiments – ensembles of 3-month-long integrations initialized on approximately November 15 of each year between 1985 and 2015 – are also used to infer impacts on simulated transport climate. As they are more computationally efficient than AMIPs since all 30 3-month integrations may be run in parallel, they are performed at both C180 and C360 (approximately quarter-degree) resolutions in order to examine the sensitivity of our results to changes in horizontal resolution.

**Table 2. GEOS Model Experiments:** Targeted GEOS model experiments based off a control experiment (row 1) were carried out to identify the influence of radiation (row 2) and changes in the remapping algorithm used since MERRA-2 (row 3), as well as their combined influence (row 4). The influence of the remapping algorithm changes is then interpreted using a simpler set of sensitivity experiments, performed using the GMAO FV core, in which only the order of the interpolation scheme used to calculate TE at output mid-layer pressure levels is altered (rows 5-7). Experiments in rows 1-4 are 30-year-long AMIPs run at C180 resolution, whereas rows 5-7 refer to 30-member 3-month-long (DJF) EMIP experiments. Both AMIPs and EMIPs are used for climate statistic evaluation (see Appendix A for more on the correspondence between the two). EMIP experiments are run at both C180 and C360 horizontal resolutions.

Experiment Name	Configuration	Experiment Type	Hor. Resolution
CTRL	Control, FV3 Core	AMIP (30 yrs.)	C180
CSRAD	Chou-Suarez (1994) Radiation (RAD)	AMIP (30 yrs.)	C180
M2REMAP	GMAO FV Core (cubic)	AMIP (30 yrs.)	C180
CSRAD+M2REMAP	Chou-Suarez (1994) RAD GMAO FV Core (cubic)	AMIP (30 yrs.)	C180
LINEAR	GMAO FV Core (linear)	EMIP (30 mem.)	C180, C360
QUADRATIC	GMAO FV Core (quadratic)	EMIP (30 mem.)	C180, C360
CUBIC	GMAO FV Core (cubic)	EMIP (30 mem.)	C180, C360

244 As shown in Appendix B, comparisons of the December-January-February (DJF)  
 245 vertical profile of tropical upwelling show excellent agreement between EMIP and AMIP  
 246 integrations carried out using the same model configuration (Appendix Figure B1). This  
 247 somewhat incidental result represents, to the best of our knowledge, the first time that  
 248 EMIP-based statistics have been shown to converge well to those from AMIPs for the  
 249 stratospheric metrics considered in this study. This suggests that EMIPs, relative to AMIPs,  
 250 may be used to provide a computationally more efficient initial assessment of the impacts  
 251 of model changes on the stratospheric circulation.

### 252 *2.2.2 Model Development Changes*

253 Moving next to the precise model development changes examined, we begin by defin-  
 254 ing a control experiment (CTRL; Table 2, row 1), which best corresponds to the blue  
 255 line shown in Figure 1. Then we define three new AMIP experiments, which aim to dis-  
 256 tinguish between the age-of-air changes resulting from changes in radiation versus changes  
 257 in the handling of the REMAP algorithm that occurred in the transition from the GMAO  
 258 to the FV3 cores (Section 3.2.1).

259 Specifically, these include experiments in which we a) replace RRTMG with the ra-  
 260 diation from Chou and Suarez (1994) (CSRAD; Table 2, row 2), b) replace the current  
 261 FV3 REMAP approach with the settings used in the GMAO FV core when running MERRA-  
 262 2 (i.e., M2REMAP; Table 2, row 3) and c) combine these two changes (CSRAD+M2REMAP;  
 263 Table 2, row 4).

264 As we show in Section 3.2.1, the M2REMAP experiment produces the largest changes  
 265 in age-of-air, compared to the experiment in which only the radiation is altered. Inter-  
 266 preting this result, however, is not straightforward since there are several differences in  
 267 the implementation of the remapping algorithm between the GMAO and FV3 cores that



268 are interdependent and, thus, difficult to isolate cleanly. To this end, in order to simplify  
 269 the problem we focus the remainder of our investigation (Section 3.2.2) on examining  
 270 a clean set of EMIP experiments that are all performed using the GMAO FV core and  
 271 that differ from each other only in terms of the order of the interpolation that is used  
 272 to calculate TE at the mid-layer pressure levels (Step 5, Table 1). More precisely, we com-  
 273 pare configurations using a linear (LINEAR; Table 2, row 5), quadratic (QUADRATIC;  
 274 Table 2, row 6) and cubic interpolation (CUBIC; Table 2, row 7) scheme, with the lat-  
 275 ter corresponding to the approach that was used in MERRA-2. To assess the robustness  
 276 of our findings to changes in horizontal resolution, all three sensitivity experiments are  
 277 run at both C180 and C360 resolutions.

278 These three numerical schemes are derived from the generic interpolation equation:

$$\mathcal{Q}(\mathcal{P}) = \sum_{k'} a_{k+k'} \mathcal{Q}_{k+k'} \quad k' = 0, \pm 1, \pm 2, \dots \quad (1)$$

279 where  $\mathcal{P}$  represents the target output location in  $\ln(p)$  and  $\mathcal{Q}_{k+k'}$  denotes the surround-  
 280 ing grid-point values at input locations. The coefficients  $a_{k+k'}$  are derived through Tay-  
 281 lor Series expansions using non-uniform grid spacing given by:

$$a_{k+k'} = \frac{\prod_m (\mathcal{P}_{k+m} - \mathcal{P})}{\prod_m (\mathcal{P}_{k+m} - \mathcal{P}_{k+k'})} \quad m = 0, \pm 1, \pm 2, \dots \quad m \neq k' \quad (2)$$

282 For the three schemes, the grid points used are: LINEAR ( $k, k-1$ ), QUADRATIC ( $k+$   
 283  $1, k, k-1$ ), and CUBIC ( $k+1, k, k-1, k-2$ ). In all cases, the grid points are chosen  
 284 such that the target location resides between layers  $k$  and  $k-1$ .

285 Note that, while the LINEAR and QUADRATIC experiments do not actually cor-  
 286 respond to any of the model versions shown in Figure 1, they highlight the large sensi-  
 287 tivity of the mean age to changes in the interpolation scheme that may otherwise seem  
 288 innocuous. They also provide further evidence of the strong influence of changes in trop-  
 289 ical lower stratospheric upwelling strength on the stratospheric mean age in GEOS.

290 Finally, in all experiments using the MERRA-2 remapping approach (i.e., M2REMAP,  
 291 CSRAD+M2REMAP, LINEAR, QUADRATIC, CUBIC) additional modifications to the  
 292 divergence damping coefficients were used so as to best ensure consistency with what was  
 293 used in MERRA-2. Specifically, these include changes to the number of layers for ver-  
 294 tical subgrid mixing, the coefficient for barotropic mode damping, the use of 2<sup>nd</sup> vs. 6<sup>th</sup>  
 295 order divergence damping and the strength of the divergence damping coefficients.

## 296 **2.3 Analysis Approach**

### 297 **2.3.1 Transport Diagnostics**

298 To diagnose the transport circulation we focus primarily on the age-of-air (Hall and  
 299 Plumb (1994)). This is inferred from an idealized global “clock” or ideal age tracer ( $\Gamma$ )  
 300 (Thiele and Sarmiento (1990)) that is defined with respect to the bottom model level  
 301 as follows: initially, the ideal age tracer is set to zero throughout the troposphere and  
 302 thereafter held to zero over the entire Earth’s surface, subject to a constant aging of 1  
 303 year/year throughout the atmosphere. We present here the statistically stationary (equi-  
 304 librated) value of  $\Gamma(r)$ , which is equal to the average time since the air at a location  $r$   
 305 in the stratosphere last contacted the Earth’s surface. In addition to the mean age, we  
 306 also show results from an idealized e90 tracer that is uniformly emitted over the entire  
 307 surface layer and decays exponentially at a rate of 90 days<sup>-1</sup> such that concentrations  
 308 greater than 125 ppb and less than 50 ppb tend to reside in the lower troposphere and  
 309 stratosphere, respectively (Prather et al. (2011)). As this tracer features strong near-  
 310 tropopause gradients and takes significantly less time to equilibrate, compared to the mean  
 311 age, it is useful for evaluating stratosphere-troposphere-exchange and transport within  
 312 the upper troposphere/lower stratosphere (Abalos et al. (2017, 2020); Orbe et al. (2020)).

Both the mean age and e90 tracers were integrated in all of the AMIP experiments shown in Figure 1 and listed in Table 2 (rows 1-4), which were run using the same idealized passive tracer package described in Orbe et al. (2017). Note that the mean age tracer was not integrated in the EMIP experiments given its much longer characteristic timescale in the stratosphere ( $\sim 3$ -5 years). As such, the EMIP simulations, which do not exceed one year, are not appropriate for evaluating the time-integrated transport characteristics reflected in the age-of-air.

In addition to carrying the idealized tracers, two of the experiments shown in Figure 1 were also run with full interactive chemistry and correspond to the two CCM1 (Phase 1 and Phase 2) integrations (red and green lines, Figure 1). Both simulations employ the same Global Modeling Initiative (GMI) chemical mechanism (Strahan et al. (2013)) and are therefore useful in evaluating the impact of age differences on real trace gas distributions. In particular, as shown in Section 3.1 results from these experiments show significant imprints of the age-of-air changes on nitrous oxide ( $\text{N}_2\text{O}$ ) and methane ( $\text{CH}_4$ ).

### 2.3.2 Circulation Diagnostics

As we show in Section 3, the changes in age-of-air across the different model versions are strongly tethered to changes in the advective component of the circulation, which we quantify using the Transformed Eulerian Mean (TEM) estimate of the Lagrangian transport of mass by the circulation. Thus, in addition to more standard Eulerian metrics of the circulation (e.g., zonal winds and temperatures), we focus on the vertical component of the TEM residual velocity, defined as  $\bar{w}^* = \bar{w} + \frac{\partial(\psi \cos\phi)}{\text{acos}\phi\partial\phi}$ , where  $\psi = \overline{v'\theta'}/\frac{\partial\theta}{\partial p}$  is the eddy stream function,  $\theta$  refers to potential temperature,  $a$  is the Earth's radius and overbars and primes denote zonal means and deviations therefrom, respectively (Andrews et al. (1987)). In addition, we interpret the behavior in  $w^*$  using the Eliassen-Palm flux divergence ( $\nabla \cdot \mathbf{F}$ ), whose horizontal ( $\mathbf{F}(\phi)$ ) and vertical ( $\mathbf{F}(p)$ ) components are respectively defined as  $\mathbf{F}(\phi) = \text{acos}\phi[\frac{\partial u}{\partial p}\psi - \overline{u'v'}]$  and  $\mathbf{F}(p) = \text{acos}\phi([\overline{f} - \frac{\partial u \cos\phi}{\text{acos}\phi\partial\phi}]\psi - \overline{u'w'})$ .

## 2.4 Observations and Reanalyses

While our focus is on interpreting and understanding the different model configurations, we incorporate observations to provide context when possible, although we do not present an exhaustive evaluation of the model's transport characteristics (for that see earlier studies including Orbe et al. (2017, 2018)). However, as the tracers are not directly integrated in MERRA-2 (with the exception of ozone), we compare against independent observational estimates. For the mean age we first compare simulated meridional age profiles at 50 hPa with values derived from in situ aircraft measurements of carbon dioxide ( $\text{CO}_2$ ), averaged in 2.5 degree latitude bins over the altitude range 19.5 to 21.5 km (Boering et al. (1996), see also Figure 5 in Hall et al. (1999)).

We also briefly evaluate impacts of transport biases on the simulated trace gas distributions for the CCM1 Phase 1 and 2 experiments. The simulated fields of methane ( $\text{CH}_4$ ) are compared with the climatologies derived for 1991–2002 from the Halogen Occultation Experiment (HALOE) on board the Upper Atmosphere Research Satellite (UARS) (Grooß and Russell III (2005)). Comparisons of simulated nitrous oxide ( $\text{N}_2\text{O}$ ) are made against climatologies derived from the Microwave Limb Sounder (MLS) on the Earth Observing System (EOS) Aura satellite. Climatologies over the same period (2005–2015) are used to evaluate both the model and the observations. We use the 190-GHz retrieval from Version 4.2 because the 640-GHz data set ends in summer 2013 due to the failure of the  $\text{N}_2\text{O}$  primary band.

For the circulation diagnostics nearly all comparisons are made relative to the MERRA-2 data assimilation (DAS) reanalysis product, noting that comparisons against ERA-5 (not shown) reveal a similar picture. One exception, however, is the vertical component

### DJF Climatological Mean Tropical Upwelling ( $w^*$ )

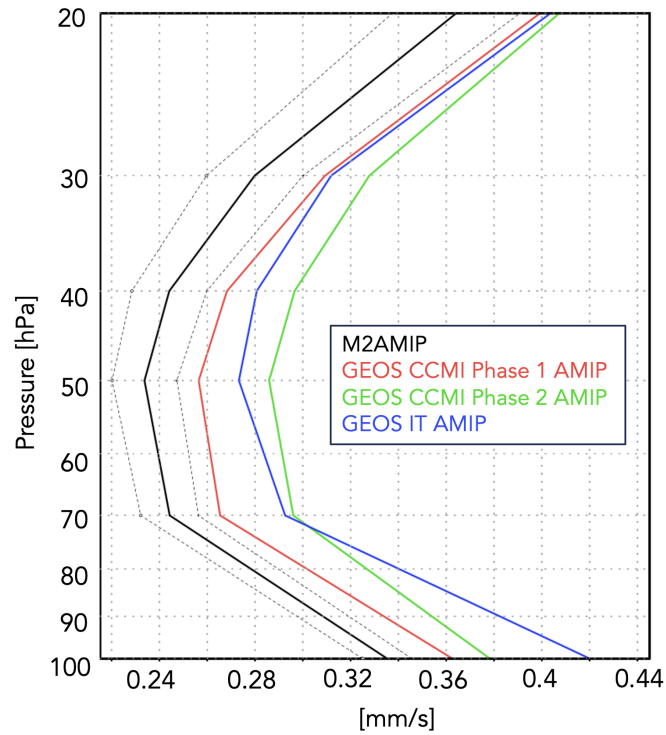


**Figure 2.** The DJF 1985-1994 climatological mean vertical residual mean velocity,  $w^*$ , averaged at each level between the turnaround latitudes for GEOS free-running AMIP simulations using the model configurations corresponding to the CCMI Phase 1 (red) and Phase 2 (green) submissions and to GEOS-IT (blue). M2AMIP is shown in black, with black dashed lines denoting  $\pm 1$  standard deviation.

of the TEM circulation ( $w^*$ ), which shows some differences in vertical structure between the MERRA-2 DAS and a 30-member ensemble of (free-running) AMIP integrations produced using the MERRA-2 model, hereafter referred to as M2AMIP (Collow et al., 2017) (Appendix Figure A1, right). As the free-running model results shown in Figure 1 show more consistency with the vertical profile of M2AMIP, not MERRA-2, we compare  $w^*$  in all free-running GEOS experiments with M2AMIP, noting that for non-derived measures (i.e., winds, temperatures), the raw MERRA-2 output is used.

The differences in  $w^*$  between M2AMIP and the MERRA-2 DAS may reflect the influence of temperature increments in the DAS (MERRA-2) which can drive spurious vertical transport in assimilated products (Weaver et al., 1993; Orbe et al., 2017). In particular, Weaver et al. (1993) showed that the imbalance between the thermal and velocity fields at the time an observation is ingested during the assimilation cycle can excite unwanted inertial-gravity wave modes that manifest strongly in the residual vertical winds. This impact of the increments may therefore explain the differences in  $w^*$ , particularly above 30 hPa, where the contribution of temperature increments to the analysis is large. We emphasize, however, that our main interest in this study is on upwelling within the lower stratosphere (i.e., 70-100 hPa), where M2AMIP and MERRA-2 agree well, as this region best correlates with the global age-of-air characteristics. As such, we reserve further exploration of the  $w^*$  differences above 50 hPa for future work.

### 3 Results

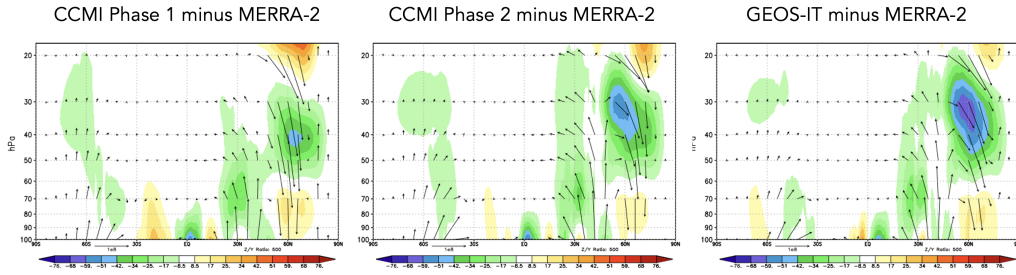
#### 3.1 Reduction of Stratospheric Mean Age in GEOS Models Since MERRA-2

We begin by interpreting the reduction in mean age exhibited in more recent model versions in terms of changes in the strength of upwelling in the tropical lower stratosphere. In particular, the reductions in  $\Gamma$  (Figure 1) are consistent with increases in the strength of lower stratospheric tropical upwelling, with  $w^*$  becoming progressively stronger in more recent model versions, relative to MERRA-2 (Figure 2). Note that these increases in  $w^*$  across model versions exceed those due to internal variability alone (black horizontal lines, Fig. 2). Furthermore, while the increases in  $w^*$  occur throughout the stratosphere, we focus on the changes occurring between 70 and 100 hPa as these are most relevant to determining the tropical upward mass flux and associated strength of the mean overturning circulation.

Though perhaps naive, the relationship between lower stratospheric upwelling and the mean age suggested by comparing Figure 1 and Figure 2 is consistent with the long-term behavior of  $\Gamma$  inferred from both historical and projected future climate simulations (Butchart et al. (2010); Abalos et al. (2021)). A strong relationship between the strength of lower stratospheric ascent and the mean age was also shown to hold in the CCMVal models (see Fig. 5.20 in J. Neu et al. (2010)). Nevertheless, it is important to note that a clear relationship between  $w^*$  and  $\Gamma$  is not a priori expected, as the age-of-air is also known to be very sensitive to mixing, which may be important in interpreting differences among the CCM Phase 1 models (Dietmüller et al. (2018)).

The differences in  $w^*$  highlighted in Figure 2 are associated with enhanced Eliassen-Palm flux convergence over NH midlatitudes (Figure 3). Increased wave convergence is evident not only within the subtropical lower stratosphere ( $< 30^\circ\text{N}$ , 50-100 hPa) but also over higher latitudes and altitudes ( $\sim 40^\circ\text{-}70^\circ\text{N}$ , 20-50 hPa). The fact that differences in extratropical wave convergence imprint on tropical upwelling is consistent with our understanding of the so-called “downward control” principle (Haynes et al. (1991)).

In particular, the strength of the residual mean streamfunction ( $\Psi^*$ ) is, via downward control, directly related to the vertically integrated eddy-induced total zonal force above that level and has contributions both from the (resolved wave) Eliassen-Palm flux

DJF Climatological Mean Eliassen-Palm Flux Divergence ( $\nabla \cdot \mathbf{F}$ )

**Figure 3.** Colors show anomalies in the DJF climatological mean Eliassen-Palm (EP) flux divergence between the CCMI Phase 1 (left), CCMI Phase 2 (middle) and GEOS-IT AMIP (right) model versions, relative to MERRA-2. Arrows denote anomalies in the vertical and meridional EP flux vectors (relative to MERRA-2).

412 divergence (Figure 3) as well as the gravity wave drag scheme’s parameterized waves (not  
 413 shown). The tropical upward mass flux – defined as  $\Psi_{\max}^* - \Psi_{\min}^*$  evaluated at the turnaround  
 414 latitudes (e.g. Rosenlof (1995)) – is therefore directly dependent on the wave forcing aloft.

415 One subtlety to note is that the wave convergence changes shown in Figure 3 oc-  
 416 cur at high latitudes and are directly associated with downwelling over the polar region.  
 417 It is then via mass balance that anomalously strong downwelling associated with enhanced  
 418 flux convergences must be accompanied by enhanced upwelling in the tropics. This in-  
 419 direct impact of higher latitude wave drag reflects an “extratropical pumping” mecha-  
 420 nism (Holton et al., 1995), which is illustrated more clearly in Section 3.2.2 in the con-  
 421 text of the LINEAR, QUADRATIC and CUBIC experiments.

422 While the reduction in  $\Gamma$  (Figure 1) of  $\sim 30\%$  at 50 hPa is significant, it is neither  
 423 clear if this change is representative of other altitudes within the stratosphere nor how  
 424 this age bias imprints on real chemical species. To this end, we begin by comparing the  
 425 full latitude-pressure distribution of changes in  $\Gamma$  and another passive tracer (e90) (Fig-  
 426 ure 4) between the CCMI Phase 1 and Phase 2 model configurations (red and green lines,  
 427 Figure 1). In particular, we find that the changes in both passive tracers – large reduc-  
 428 tions in  $\Gamma$  within both hemispheres (Fig. 4, top right) and increased values of e90 within  
 429 the lower stratosphere (Fig. 4, bottom right) – are reflective of an overall increase in the  
 430 strength of the transport circulation. This is highlighted in the CCMI Phase 2 – 1 model  
 431 differences for the passive tracer distributions (Fig. 4, right panels) which are shown in  
 432 the absence of robust observational constraints of  $\Gamma$  at higher altitudes (or any obser-  
 433 vational constraints for e90, for that matter). The reduced/increased stratospheric bur-  
 434 dens of the age and e90 tracers are consistent with stronger upwelling in the CCMI Phase  
 435 2 model configuration (Figure 2).

436 While the observational constraints on  $\Gamma$  presented in Figure 1 and the departure  
 437 of  $w^*$  away from MERRA-2 suggest that transport properties of the newer model con-  
 438 figurations are moving in the wrong direction, it is relevant to ask whether or not the  
 439 trace gas satellite measurements also support this conclusion. Indeed, comparisons with  
 440 observations show larger biases in  $\text{N}_2\text{O}$  (Fig. 5, top panels) and  $\text{CH}_4$  (Fig. 5, bottom pan-  
 441 els), increasing from 10% to 30% in the CCMI Phase 2 model configuration, depending  
 442 on the species. Recall that the same chemistry mechanism is used in both CCMI Phase  
 443 1 and 2 simulations.

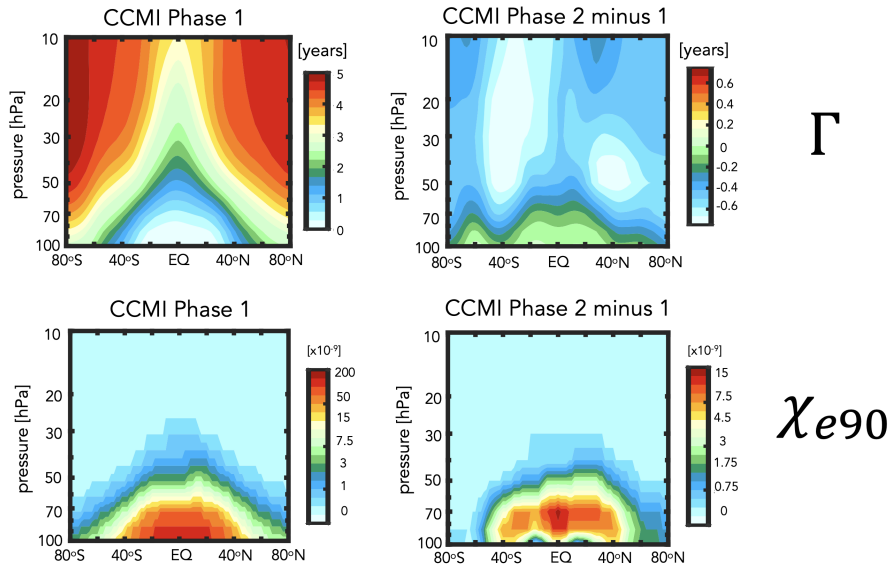


**Figure 4.** The climatological mean (2000-2010) distribution of the mean age-of-air ( $\Gamma$ ) (left, top) and e90 idealized tracers (left, bottom) for the CCMI Phase 1 model configuration. Climatological differences between the CCMI Phase 2 and Phase 1 model configurations are shown in the right panels. Note that a nonlinear colorbar has been used in the e90 subplots.

444 The patterns of the trace gases biases are generally consistent with the biases in  
 445 the mean age (Fig. 4). This comports with well-known correlations between the mean  
 446 age and stratospheric trace gases, reinforcing the fact that model transport inaccuracies  
 447 can significantly affect simulations of important long-lived chemical species in the strato-  
 448 sphere (Hall et al. (1999)).

449 The fact that the mean age changes have a significant imprint on the simulated trace  
 450 gases is consequential for the GEOS-R21C system. However, the configurations shown  
 451 in Fig. 1-5 differ in many respects (physics, resolution, radiation, FV remapping algo-  
 452 rithm) and it is difficult to meaningfully interpret what is driving the changes in  $w^*$  (and  
 453 the tracers). We therefore move next to the targeted model experiments (Table 2) in or-  
 454 der to interpret the model development steps that resulted in these transport circula-  
 455 tion changes.

## 456 3.2 Identifying Drivers of Upwelling and Tracer Changes Since 457 MERRA-2

### 458 3.2.1 Radiation versus REMAP Algorithm

459 As discussed in Section 2, among the model changes that were made since MERRA-  
 460 2, the changes in radiation and the FV remapping algorithm are most likely to directly  
 461 have impacted the stratospheric circulation. We therefore begin by assessing which of  
 462 these changes dominates the decreases in  $\Gamma$  shown in Figure 1.

463 Figure 6 shows the distribution of  $\Gamma$  for experiments in which the longwave, short-  
 464 wave, and REMAP updates since MERRA-2 have successively been undone. Relative  
 465 to the control experiment (CTRL; Table 2, row 1), the transition back to Chou and Suarez  
 466 (1994) in the shortwave and Chou (1990, 1992) in the longwave results in an increase in  
 467 the mean age of  $\sim 0.5$  years throughout the stratosphere (CSRAD; Table 2, row 2). Though

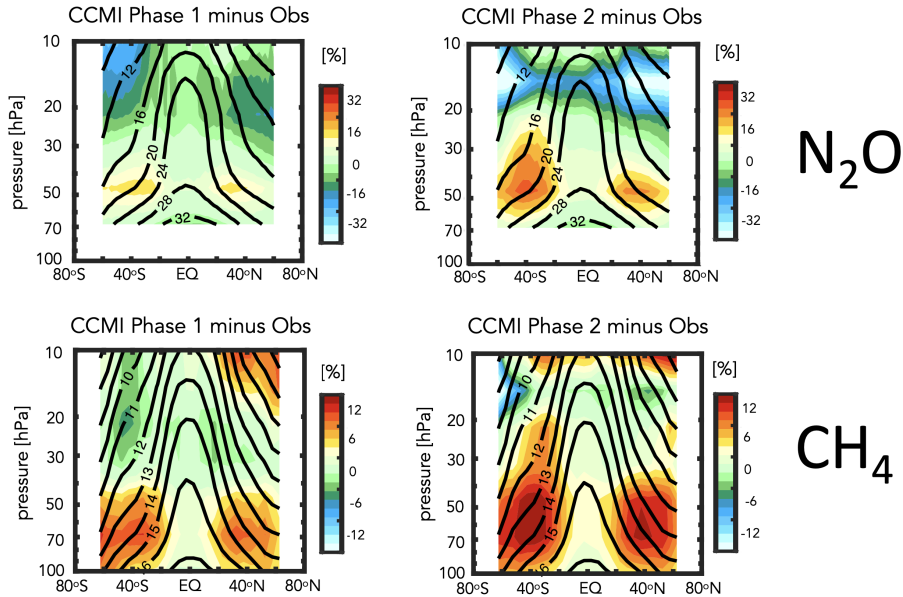


**Figure 5.** Colors shown anomalies in the simulated distributions of nitrous oxide ( $\text{N}_2\text{O}$ ) (top) and methane ( $\text{CH}_4$ ) (bottom), relative to the MLS and HALOE observed values, respectively, for the CCMI Phase 1 (left) and Phase 2 (right) GEOS model configurations. Climatological mean observed values are shown in the black contours.

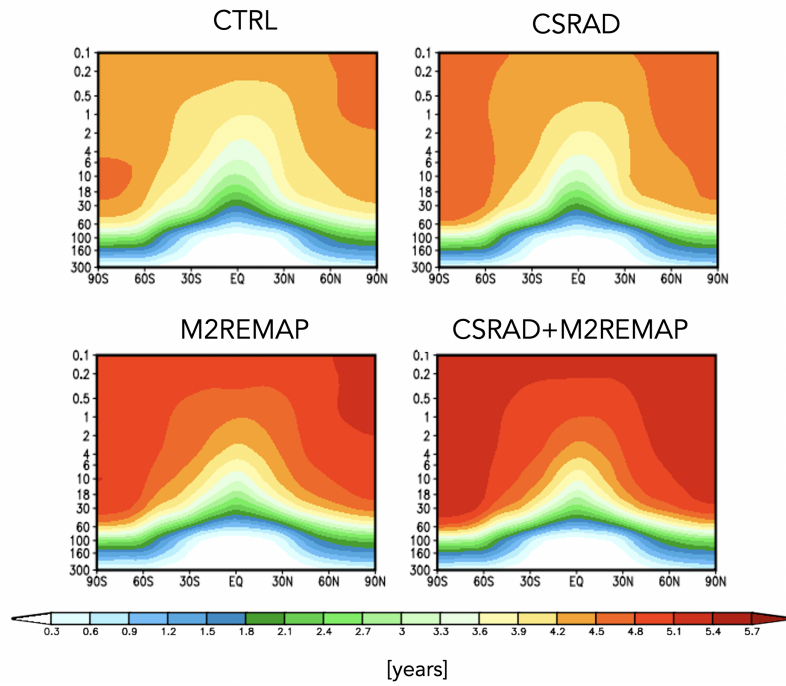
468 significant, this change in  $\Gamma$  is smaller than the change that results from applying the  
 469 remapping approach used in MERRA-2 (M2REMAP; Table 1; row 3), in which the mean  
 470 age increases by  $\sim 1$  year. The combined impacts of both changes (CSRAD+M2REMAP;  
 471 Table 1 row 4) is roughly linear, with age values of  $\sim 5.5$  years over high latitudes at 50  
 472 hPa, consistent with the values simulated by the GEOS-CTM MERRA-2 integration (black  
 473 line, Figure 1) and with the CCMI Phase-1 version of the model (red line, Figure 1).

474 Next we ask if the behavior of  $\Gamma$  exhibited in Figure 6 can be interpreted in terms  
 475 of changes in the strength of lower stratospheric tropical upwelling and extratropical wave  
 476 convergence, as our previous analysis of the CCMI experiments suggested. Indeed, Figure  
 477 7 shows that values of upwelling decrease in the CSRAD and M2REMAP experiments,  
 478 relative to the CTRL integration. The increase in upwelling resulting from both changes  
 479 (CSRAD+M2REMAP) is still larger, consistent with the larger age decreases in that exper-  
 480 iment. This change in the behavior of  $w^*$  within the tropical stratosphere can be inter-  
 481 preted in terms of changes in the Eliassen Palm flux convergence over NH midlati-  
 482 tudes (not shown), which features smaller values in the CSRAD, M2REMAP (and CSRAD+  
 483 MSREMAP) experiments. Note that our examination of the changes in  $w^*$  are derived  
 484 from EMIP integrations, which we showed previously converge (for DJF) to the statis-  
 485 tics derived from corresponding AMIP experiments.

### 486 3.2.2 FV REMAP Algorithm: Sensitivity of Climate Statistics

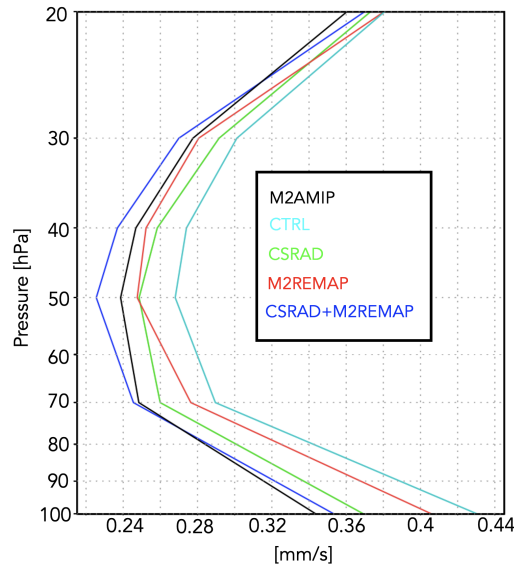
487 Having shown in the previous section that the largest changes in the mean age were  
 488 realized through the differences in implementation of the remapping algorithm between  
 489 the GMAO FV core used in MERRA-2 and in current FV3 core configurations, we now  
 490 investigate further the sensitivity of the transport circulation to the choice of remapping

### Annual Climatological Mean Stratospheric Mean Age ( $\Gamma$ )



**Figure 6.** Colors show the simulated 2000-2010 climatological annual mean distributions of the mean age-of-air ( $\Gamma$ ) for the CTRL (top left; Table 1, row 1), CSRAD (top right; Table 1, row 2), M2REMAP (bottom left; Table 1, row 3) and combined CSRAD+M2REMAP (bottom right; Table 1, row 4) experiments.



DJF Climatological Mean Tropical Upwelling ( $w^*$ )

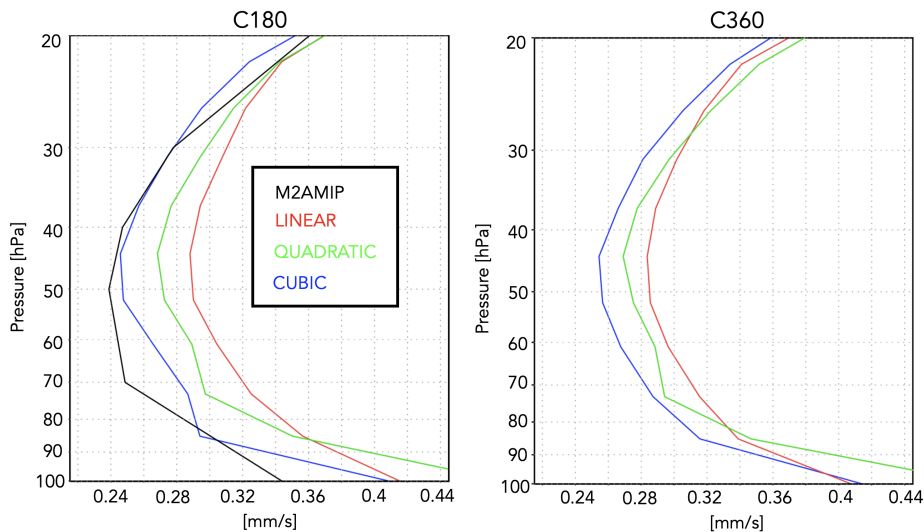
**Figure 7.** The DJF 1985-2015 climatological mean vertical residual mean velocity,  $w^*$ , averaged at each level between the turnaround latitudes for the CTRL (cyan line; Table 2, row 1), CSRAD (green line; Table 2, row 2), M2REMAP (red line; Table 2, row 3) and combined CSRAD+M2REMAP (blue line; Table 2, row 4) experiments. M2AMIP is shown in black.

491 interpolation scheme. In particular, we compare simulations run with the GMAO FV  
 492 core in which total energy is calculated at new mid-layer pressures using cubic, quadratic  
 493 and linear interpolation prior to the aposterior integral conservation (Table 2, rows 5-  
 494 7). In addition, in this section we seek to understand how the changes in the Eliassen-  
 495 Palm flux convergence over NH midlatitudes arise via analysis of the large-scale wind  
 496 structure.

497 Figure 8 (left panel) shows a clear sensitivity in tropical upwelling to the choice of  
 498 interpolation scheme, with  $w^*$  progressively increasing in strength moving from the CU-  
 499 BIC to QUADRATIC to LINEAR schemes. This sensitivity is robust across horizontal  
 500 resolutions as the same suite of experiments performed at C360 exhibit the same sensi-  
 501 tivity (Fig. 8, right panel). While no current model version actually employs a linear  
 502 scheme, this suite of experiments highlights the strong sensitivity to choice of interpo-  
 503 lation scheme within the remapping algorithm; to the best of our knowledge, this result  
 504 has not been reported in the literature.

505 Furthermore, as we show next, this clean set of experiments allow us to inquire mech-  
 506 anistically into the processes that are driving the changes in wave convergence over mid-  
 507 latitudes, unencumbered by differences in horizontal resolution, physics, etc.

508 Interestingly, the increases in  $w^*$  moving from the CUBIC to QUADRATIC schemes  
 509 not only manifests in free-running AMIP simulations, but also in AMIP simulations in  
 510 which GEOS is constrained (or replayed, following Orbe et al. (2017)) to MERRA-2 me-  
 511 teorological fields, using the MERRA-2 GMAO cubic interpolation (Fig. 9, blue line)  
 512 and the GFDL FV core remapping approach (Fig. 9, red line). While there is a general  
 513 increase in  $w^*$  in the former, however, both simulations, lie within the range of MERRA2-  
 514 DAS, suggesting that replay does act to ameliorate some of the upwelling biases man-  
 515 ifest in the underlying unconstrained models. While not the focus of this study, this im-

DJF Climatological Mean Upwelling ( $w^*$ )

**Figure 8.** The DJF 1985-2015 climatological mean vertical residual mean velocity,  $w^*$ , averaged at each level between the turnaround latitudes for the LINEAR (red line; Table 2, row 5), QUADRATIC (green line; Table 2, row 6) and CUBIC (blue line; Table 2, row 7) experiments. M2AMIP is shown in black. Results from C180 and C360 EMIP experiments are shown in the left and right panels, respectively.

516 pact of the remapping approach on simulations run in both replay and DAS mode will  
 517 be examined further in future work.

518 Consistent with our expectations based on the analysis of the previous experiments,  
 519 the drivers of the changes in  $w^*$  are related to increased wave convergence moving from  
 520 the CUBIC to QUADRATIC to LINEAR schemes (Figure 10). Over extratropical lat-  
 521 itudes, the zonal force associated with this enhanced wave convergence is associated with  
 522 enhanced downwelling at high latitudes that, through mass balance, is accompanied by  
 523 enhanced upwelling in the tropics. This indirect impact of higher latitude wave drag is  
 524 evident in Appendix Figure C1, which shows stronger upwelling/downwelling in the LIN-  
 525 EAR and QUADRATIC experiments over the tropics/polar region.

526 Next we exploit the fact that these experiments only differ with respect to the in-  
 527 terpolation scheme in order to inquire further into the drivers of the wave convergence  
 528 changes. To this end, Figure 11 compares profiles of the zonal mean zonal wind between  
 529 the CUBIC, QUADRATIC and LINEAR experiments, averaged over the region of en-  
 530 hanced wave convergence (i.e. 20°N-60°N). The experiments featuring stronger wave con-  
 531 vergence (LINEAR and QUADRATIC) are also simulations with stronger zonal winds,  
 532 relative to MERRA-2, especially above 70 hPa. This change in winds occurs at both C180  
 533 (Fig. 10, left panel) and C360 (Fig. 10, right panel) resolutions.

534 Structurally, the increase in zonal wind strength over northern extratropical mid-  
 535 latitudes is reflective of a poleward shift in the zonal winds as the critical latitude, i.e.  
 536 where the zonal wind is zero, shifts northward in the QUADRATIC and, especially, LIN-  
 537 EAR integrations, relative to the CUBIC experiment (Figure 12). Since stationary waves  
 538 only propagate in westerly zonal flow, the latitude where zonal flow is zero acts a bound-  
 539 ary for wave propagation (Hardiman et al. (2014)). As a result, this shift in critical lat-

### DJF Climatological Mean Tropical Upwelling ( $w^*$ )

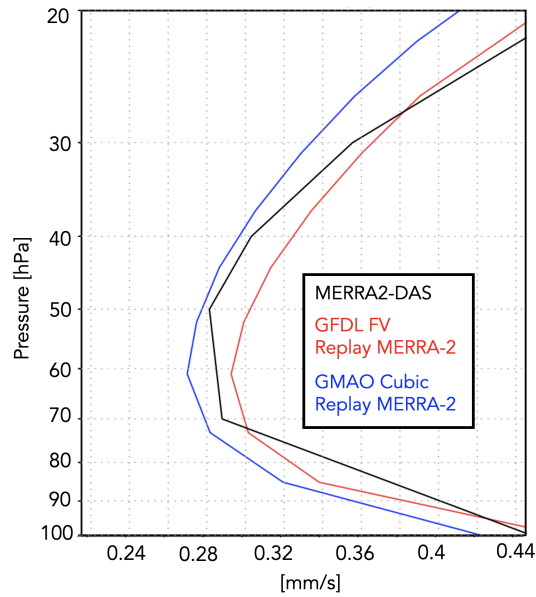


**Figure 9.** The DJF 2005-2015 climatological mean vertical residual mean velocity,  $w^*$ , averaged at each level between the turnaround latitudes for two GEOS replay AMIP simulations constrained with MERRA-2 meteorological fields using remapping approaches from the MERRA-2 GMAO cubic core (blue line) and the GFDL FV core (red line). MERRA-2 DAS is shown in black.

### DJF Climatological Mean Eliassen-Palm Flux Divergence ( $\nabla \cdot F$ )

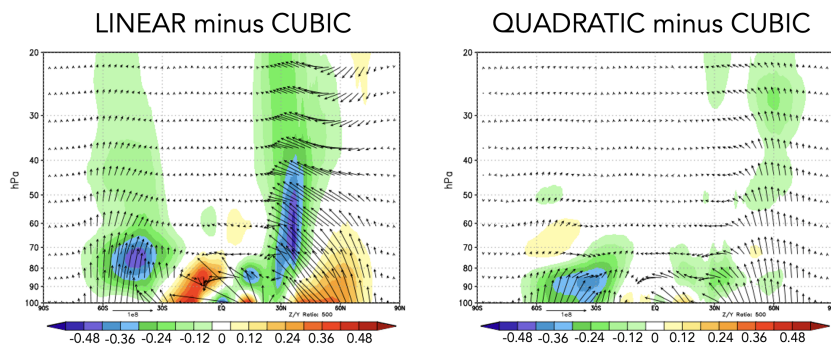


**Figure 10.** Colors shown anomalies in the DJF 1985-2015 climatological mean Eliassen-Palm (EP) flux divergence in the LINEAR (left) and QUADRATIC (right) experiments, relative to the CUBIC model experiment. Arrows denote anomalies in the vertical and meridional EP flux vectors.

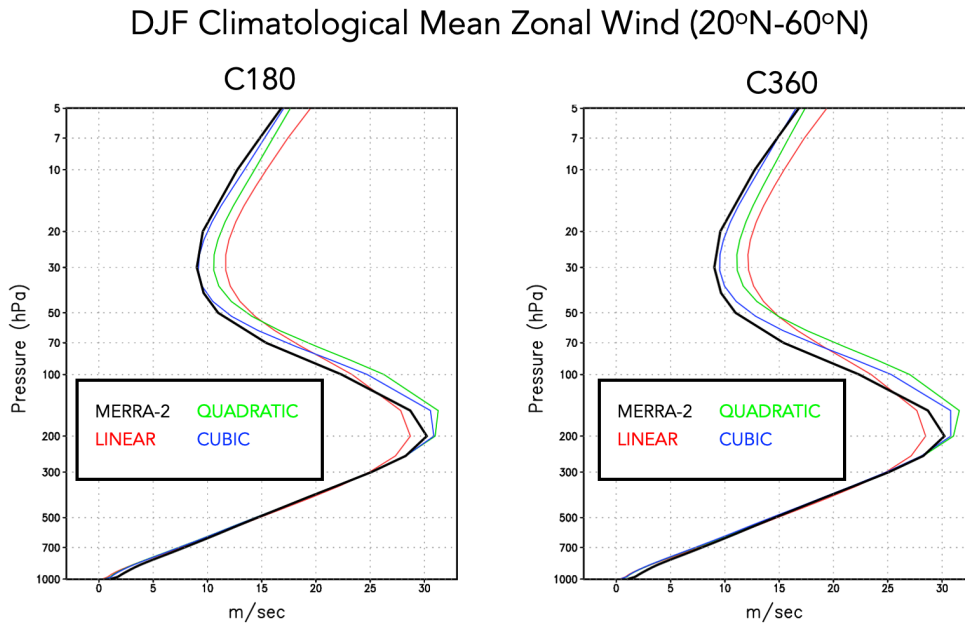


**Figure 11.** Vertical profiles of the DJF 1985-2015 climatological mean zonal mean zonal winds in the LINEAR (red), QUADRATIC (green) and CUBIC (blue) experiments, averaged between 20°N and 60°N. MERRA-2 is shown in the black line. Results for both C180 (left) and C360 (right) experiments are shown.

540 itude results in enhanced wave propagation and convergence over middle and high lat-  
 541 itudes.

542 Figures 11 and 12 highlight how the changes in zonal winds in the LINEAR and  
 543 QUADRATIC experiments reflect a degradation in model skill, relative to MERRA-2,  
 544 throughout the entire stratosphere. The changes in upwelling, mean age, chemical trace  
 545 gases and zonal winds thus provide a coherent and self-consistent picture suggestive of  
 546 a degradation in the representation of the stratospheric circulation since MERRA-2. That  
 547 is, an increased bias in the stratospheric northern zonal winds are, via their influence on  
 548 wave convergence, compromising changes in the strength of the mean meridional over-  
 549 turning circulation and its impact on composition. It is interesting to note that the wind  
 550 biases also extend into the troposphere and show degraded skill relative to MERRA-2  
 551 in the LINEAR and QUADRATIC experiments (Figure 12). Examination of other fields  
 552 (i.e. tropopause biases, Appendix Figure D1) present somewhat more of a nuanced story  
 553 that depends more sensitively on latitude and season considered. The improvements in  
 554 the zonal winds, however, are most relevant for setting the upwelling characteristics within  
 555 the tropical lower stratosphere via their influence on wave propagation into that region.

556 Finally, to better understand why these impacts on the winds have such a conse-  
 557 quence for the wave convergence properties within the stratosphere, next we examine the  
 558 zonal structure of these biases in the middle stratosphere (Figure 13). This reveals that  
 559 the enhanced winds in the LINEAR (and, to a lesser extent, QUADRATIC) integrations  
 560 are concentrated over the North Pacific at both C180 (Fig. 12, left) and C360 (Fig. 12,  
 561 right) resolutions (a similar picture emerges within the troposphere, not shown). As this  
 562 region is the primary region dominating the stationary component of the upward flux  
 563 of vertical wave activity (Plumb (1985), see their Figure 4) it is perhaps not surprising  
 564 that this region is having a profound impact on the mean overturning circulation. Again,

## DJF Climatological Zonal Mean Zonal Wind Anomalies Relative to MERRA-2

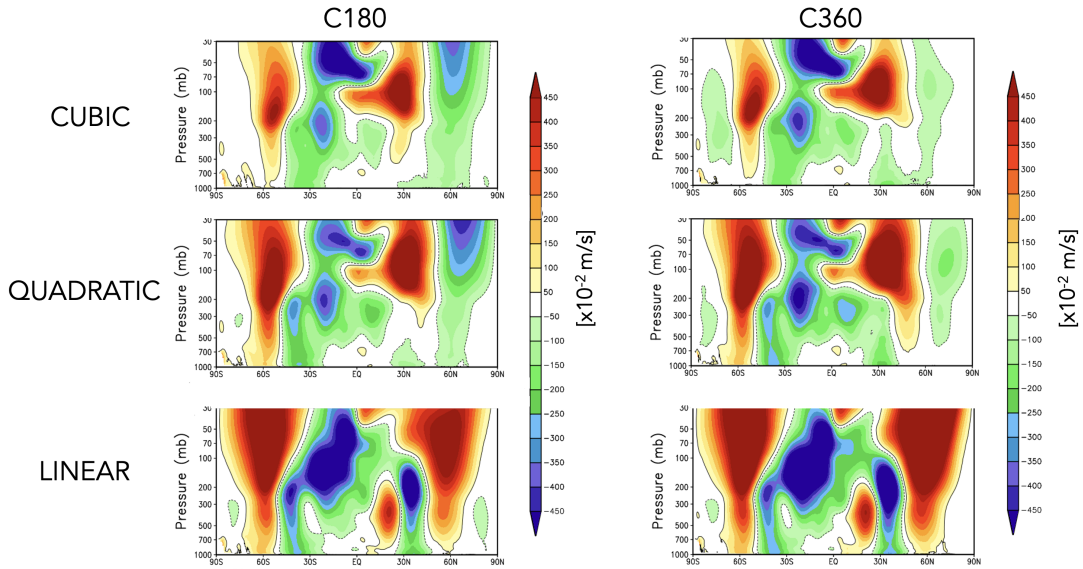


**Figure 12.** Colors shown anomalies in the DJF 1985-2015 climatological mean zonal mean zonal winds in the CUBIC (top), QUADRATIC (middle) and LINEAR (bottom) experiments, relative to MERRA-2. Results for both C180 (left) and C360 (right) experiments are shown.

565 as with the zonal mean wind changes, the increases in wind strength over the North Pa-  
 566 cific represent degraded model skill relative to MERRA-2. Note that comparisons with  
 567 ERA-5 reveal a similar bias (not shown).

#### 568 4 Conclusions

569 Here we have performed an analysis aimed at understanding differences in the rep-  
 570 resentation of the stratospheric circulation in recent candidate systems for GEOS-R21C,  
 571 relative to older versions of GEOS similar to the model used to produce MERRA-2. Us-  
 572 ing targeted experiments oriented at disentangling various model development updates,  
 573 we have identified a key role played by changes in the implementation of the remapping  
 574 algorithm within the model's finite-volume dynamical core. Our key results are as fol-  
 575 lows:

576 #1. The stratospheric mean age-of-air in GEOS is sensitive to the degree of the  
 577 interpolation scheme that is used to calculate layer-mean values of total energy, U, V and  
 578 tracers. Different treatment of the vertical remapping algorithm result in mid-stratospheric  
 579 (50 hPa) age-of-air differences of  $\sim 1$  year over high latitudes, or about 30% climatolog-  
 580 ical mean values.

581 #2. The increased age-of-air biases in more recent GEOS configurations are reflected  
 582 in the increased biases in simulated trace gases, including  $\text{CH}_4$  and  $\text{N}_2\text{O}$ .

583 #3. The age-of-air sensitivities reflect, to first order, changes in the strength of tropi-  
 584 cal upwelling associated with the Brewer-Dobson circulation which are in turn are driven  
 585 by changes in EP flux convergence over northern midlatitudes. Changes in wave conver-  
 586 gence reflect shifts in (critical lines of) wave propagation that originate in the troposphere  
 587 over the Pacific Ocean, a region of strong upward wave activity.

### DJF Climatological 30 hPa Zonal Wind Anomalies Relative to MERRA-2

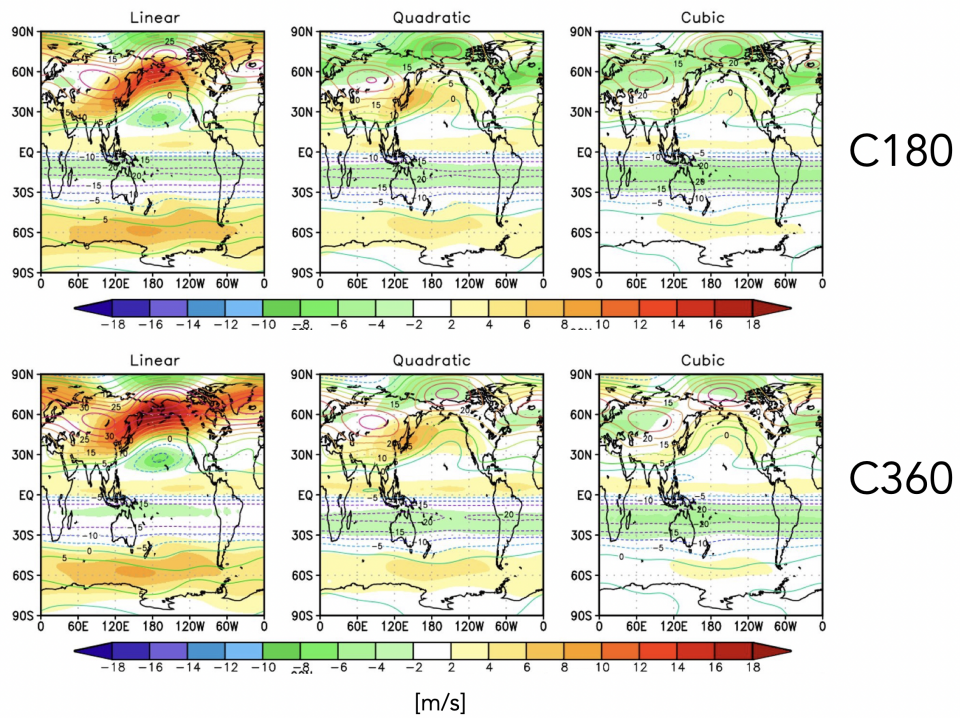


**Figure 13.** Colors shown anomalies in the DJF 1985-2015 climatological mean zonal winds at 30 hPa in the CUBIC (right), QUADRATIC (middle) and LINEAR (left) experiments, relative to MERRA-2. Results for both C180 (top) and C360 (bottom) experiments are shown.

588 #4. The degradation of upwelling statistics manifest in AMIPs, also translate to  
 589 degradations in configurations of GEOS in which the meteorological fields are constrained  
 590 or “replayed” to MERRA-2.

591 Interestingly, preliminary analysis suggests that our findings may also translate to  
 592 replay configurations of GEOS (Figure 9), although the effect is muted, relative to free-  
 593 running configurations. As a rigorous evaluation of the stratospheric circulation in re-  
 594 play and DAS configurations is beyond the scope of the current study, future work will  
 595 therefore focus on assessing the extent to which the free-running model biases reported  
 596 here are expressed when the model is run in data assimilation mode. It also bears em-  
 597 phasizing that our findings do have immediate implications for the (free-running) sub-  
 598 seasonal forecast and coupled chemistry climate applications of the GEOS model cur-  
 599 rently in operation.

600 In addition to its implications for GEOS, our results more generally highlight the  
 601 key role played by model numerics in transport (e.g., Rood (1987)). The sensitivities in  
 602 the age-of-air documented herein are also consistent in spirit with the findings in Gupta  
 603 et al. (2020) who showed significant age differences occurring between spectral versus  
 604 finite-volume numerics. Our results, however, suggest that there remain large sensitiv-  
 605 ities even within a given (FV) dynamical core.

606 Looking forward, our findings support and build on the recommendation proposed  
 607 in Gupta et al. (2020) for the construction of dynamical core benchmark tests aimed at  
 608 determining how underlying AGCM numerics impact climatological transport proper-  
 609 ties. In particular, in addition to the age-of-air, the authors propose a range of strato-  
 610 spheric circulation diagnostics that should be evaluated including the zonal mean zonal  
 611 winds, eddy temperature variance and zonal spectra of eddy kinetic energy. Our anal-  
 612 ysis reveals an important role to be played by the climatological zonal mean wind struc-  
 613 ture as it impacts wave convergence over midlatitudes; we therefore also recommend ex-  
 614 plicit consideration of the Eliassen Palm flux convergence and tropical upwelling ( $w^*$ )  
 615 fields as they may be crucial for interpreting age-of-air changes.

616 One somewhat incidental – but practical - result from our analysis is that the statis-  
 617 tics of  $\nabla \cdot \mathbf{F}$  and  $w^*$  are well approximated by ensembles of so-called EMIP integrations.  
 618 As these are substantially easier to run than AMIPs these could provide a “first pass”  
 619 when evaluating new proposed model development changes, without the immediate need  
 620 to integrate AMIP-style experiments. We emphasize, however, that this statement should  
 621 only apply to a first stage in model development as the age-of-air will reflect the time  
 622 integrated impacts of both advection and mixing.

623 Finally, we conclude by noting that, while we have focused on sensitivities within  
 624 the FV remapping algorithm, our results have highlighted important sensitivities to changes  
 625 in radiation and, to a lesser extent, changes in parameterized convection. Though not  
 626 the dominant drivers of the age-of-air changes identified here, the former could poten-  
 627 tially influence the age both directly through changes in thermal structure and indirectly  
 628 by modifying wave propagation and/or generation in the troposphere.

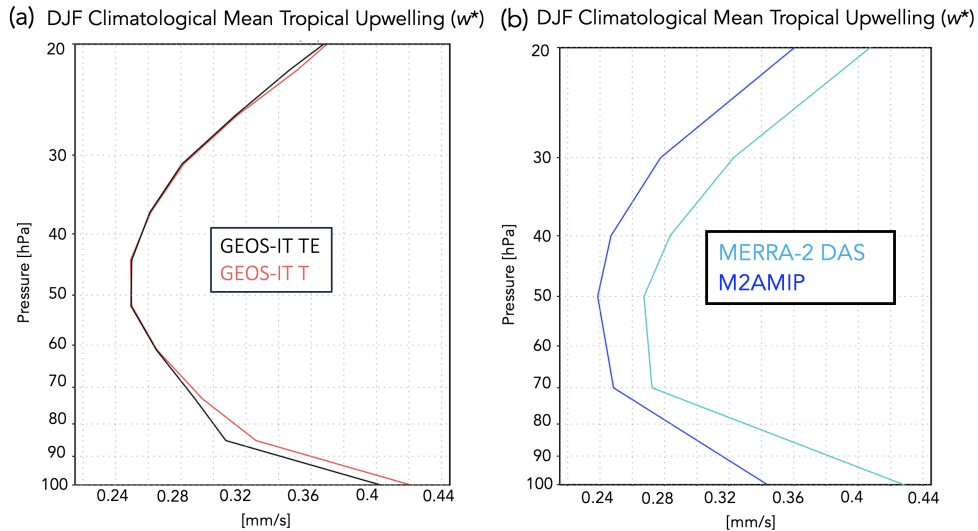


**Figure A1.** The DJF 1985–2015 climatological mean vertical residual mean velocity,  $w^*$ , averaged at each level between the turnaround latitudes compared between two experiments remapping to temperature (T) (red) versus total energy (TE) (black) (a) and between MERRA-2 DAS (cyan) and the M2AMIP ensemble (blue) (b). The underlying model code is consistent with the Version 5.29.4 GEOS-IT model.

## 629 Appendix A Sensitivities in Calculation of TEM Upwelling

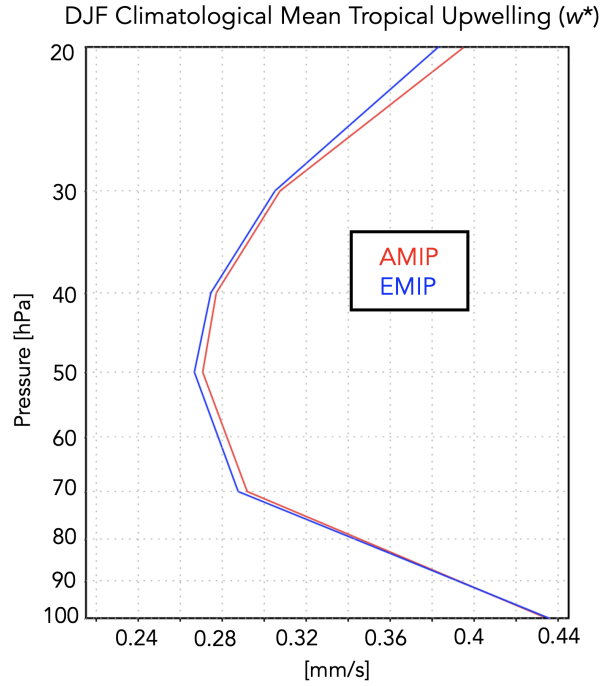
630 There are various aspects of the calculation of the TEM circulation that warrant  
 631 further comment. First, whereas the modeling experiments listed in Table 2 (rows 5–7)  
 632 focus on the sensitivity of Step 5 within the GMAO FV core remapping algorithm to the  
 633 choice of interpolation scheme, another difference between the GMAO and FV3 core remap-  
 634 ping approaches is the use of TE versus T, respectively. To test the impact of this dif-  
 635 ference, we ran a new experiment which is identical to the CUBIC experiment (Table  
 636 2, row 7), except that T is remapped from input layer mean pressure locations to stan-  
 637 dard output layer mean locations directly using cubic interpolation (i.e., no computa-  
 638 tion of TE or a-posteriori energy conservation applied). Appendix Figure A1a shows that  
 639 this has little impact on the strength of tropical upwelling, suggesting that the  $w^*$  dif-  
 640 ferences associated with changes in the remapping algorithm are dominated by sensitiv-  
 641 ities to the choice of interpolation scheme, not the use of TE versus T.

642 Second, the vertical component of the TEM circulation ( $w^*$ ) shows some differences  
 643 in vertical structure between MERRA-2 and the 30-member M2AMIP ensemble (Ap-  
 644 pendix Figure A1b). This difference in vertical structure appears to reflect a difference  
 645 between DAS and free-running configurations of the model, since other DAS configura-  
 646 tions share a similar vertical structure (not shown). Given this difference, we ensure as  
 647 apples-to-apples a comparison of simulated TEM velocities by comparing all AMIP re-  
 648 sults to other AMIPs, and vice versa for the few selected DAS results.

## 649 Appendix B Correspondence between EMIP and AMIP Upwelling

650 Appendix Figure B1 shows the close correspondence in DJF climatological mean  
 651  $w^*$ , averaged at each level between the turnaround latitudes, from AMIP and EMIP ex-



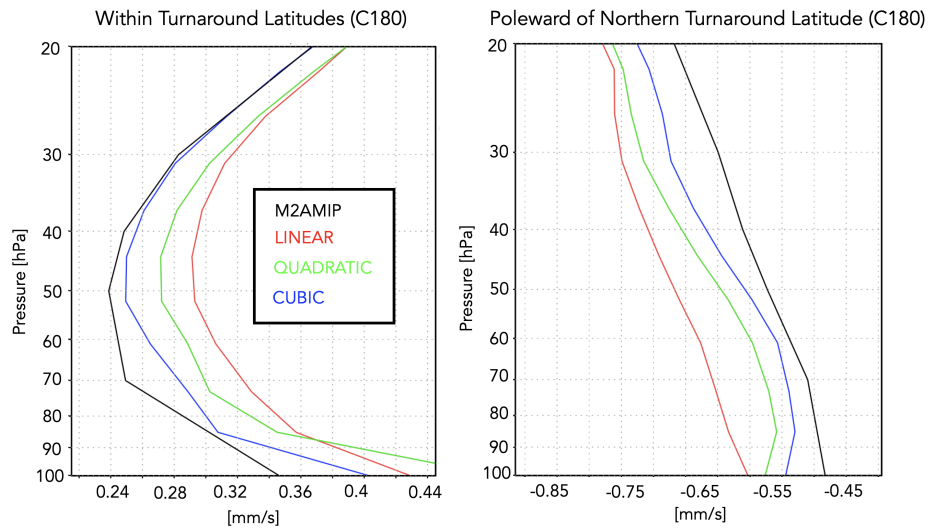


**Figure B1.** The DJF 1985-2015 climatological mean vertical residual mean velocity,  $w^*$ , averaged at each level between the turnaround latitudes for the CTRL experiment (Table 2, row 1). Results based on a 30-year-long AMIP experiment (red line) and a 30-member ensemble of three-month-long EMIP experiments (blue line) are shown.

652 periments using the same model configuration. This good agreement in upwelling is used  
 653 to justify the analysis of the EMIP experiments listed in Table 2 (rows 5-7).

## 654 **Appendix C Changes in Tropical and High Latitude Upwelling**

655 Appendix Figure C1 compares the behavior in residual mean upwelling among the  
 656 LINEAR, QUADRATIC and CUBIC experiments over the latitudes between the (tropi-  
 657 cal) turnaround latitudes (left) and poleward of the northern turnaround latitude (right).  
 658 The ordering among experiments in both regions reflects how increases in downwelling  
 659 at high latitudes are, through mass balance, accompanied by enhanced upwelling in the  
 660 tropics.

DJF Climatological Mean Upwelling ( $w^*$ )

**Figure C1.** Left: The DJF 1985-2015 climatological mean vertical residual mean velocity,  $w^*$ , averaged at each level between the turnaround latitudes for the LINEAR (red line; Table 2, row 5), QUADRATIC (green line; Table 2, row 6) and CUBIC (blue line; Table 2, row 7) experiments. M2AMIP is shown in black. Right: As in left panel, except averaged over latitudes poleward of the northern turnaround latitude. Results in both panels are shown for C180 experiments.

661 **Appendix D Tropopause Pressure**

662 Appendix Figure D1 compares boreal winter tropopause pressure and temperature  
 663 among the LINEAR, QUADRATIC and CUBIC experiments, relative to MERRA-2.

## DJF Climatological Mean Tropopause

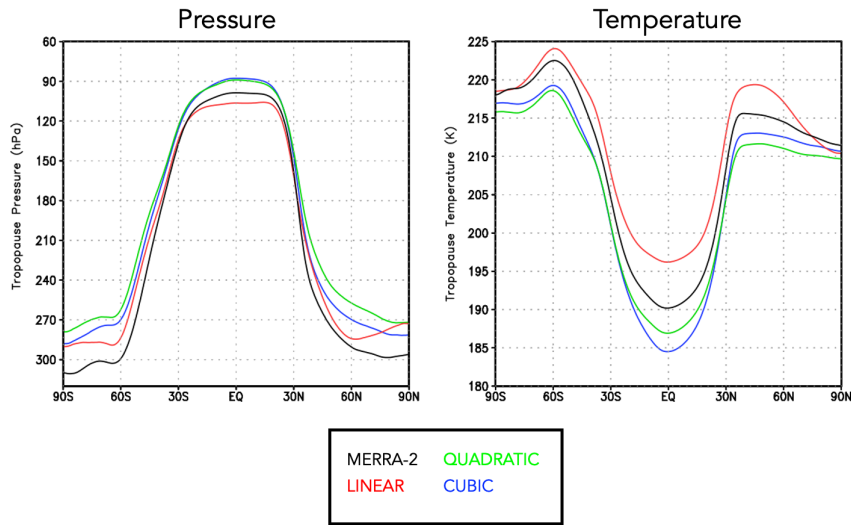


**Figure D1.** The DJF 1985-2015 climatological mean tropopause pressure (left) and temperature (right) in the CUBIC (blue), QUADRATIC (green) and LINEAR (red) experiments. MERRA-2 is shown in black. Results are shown for the C180 experiments.

### 664 Acronyms

- 665 **AMIP** Atmospheric Model Intercomparison Project
- 666 **CH<sub>4</sub>** methane
- 667 **CCMs** chemistry climate models
- 668 **CCMI** Chemistry Climate Modeling Initiative
- 669 **CCMVal** Chemistry Climate Model Validation
- 670 **CO<sub>2</sub>** carbon dioxide
- 671 **CTRL** control
- 672 **CTM** chemistry transport model
- 673 **DAS** Data assimilation
- 674 **DJF** December-January-February
- 675 **EMIP** ensemble AMIP
- 676 **EOS** Earth Observing System
- 677 **EP** Eliassen-Palm
- 678 **FV** finite-volume
- 679 **FP** Forward Processing
- 680 **GEOS** Global Earth Observing System
- 681 **GEOS-R21C** GEOS Retrospective analysis for the 21<sup>st</sup> Century
- 682 **GMI** Global Modeling Initiative
- 683 **HALOE** Halogen Occultation Experiment
- 684 **MERRA-2** Modern-Era Retrospective Analysis for Research and Applications v2
- 685 **MLS** Microwave Limb Sounder
- 686 **N<sub>2</sub>O** nitrous oxide
- 687 **NH** northern hemisphere
- 688 **PPM** piecewise parabolic
- 689 **RRTMG** Rapid Radiative Transfer Model for GCMS

690 **SW** shortwave  
 691 **TE** total energy  
 692 **TEM** Transformed Eulerian Mean  
 693 **UARS** Upper Atmosphere Research Satellite

## 694 **Open Research Section**

695 TBD

## 696 **Acknowledgments**

697 C.O. thanks William Putnam and Lawrence Coy for their insight which helped in inter-  
 698 preting the results and guiding experimental design. The authors also thank the high-  
 699 performance computing resources provided by NASA’s Advanced Supercomputing (NAS)  
 700 Division and the NASA Center for Climate Simulation (NCCS) as well as NASA’s Mod-  
 701 eling, Analysis and Prediction (MAP) program, which supports the Global Modeling As-  
 702 simulation Office and core chemistry-climate and chemistry-modeling activities.

## 703 **References**

- 704 Abalos, M., Calvo, N., Benito-Barca, S., Garny, H., Hardiman, S. C., Lin, P., ...  
 705 others (2021). The Brewer–Dobson circulation in CMIP6. *Atmospheric*  
 706 *Chemistry and Physics*, *21*(17), 13571–13591.
- 707 Abalos, M., Orbe, C., Kinnison, D. E., Plummer, D., Oman, L. D., Jöckel, P., ...  
 708 others (2020). Future trends in stratosphere-to-troposphere transport in CCM1  
 709 models. *Atmospheric Chemistry and Physics*, *20*(11), 6883–6901.
- 710 Abalos, M., Randel, W. J., Kinnison, D. E., & Garcia, R. R. (2017). Using the  
 711 artificial tracer e90 to examine present and future UTLS tracer transport in  
 712 WACCM. *Journal of the Atmospheric Sciences*, *74*(10), 3383–3403.
- 713 Andrews, D., Holton, J., & Leovy, C. (1987). Middle Atmosphere Dynam-  
 714 ics. *Academic Press*, *60*, 489. doi: 10.1175/1520-0469(2003)060<0103:  
 715 CEOOAL>2.0.CO;2
- 716 Boering, K. A., Wofsy, S., Daube, B., Schneider, H., Loewenstein, M., Podolske, J.,  
 717 & Conway, T. (1996). Stratospheric mean ages and transport rates from obser-  
 718 vations of carbon dioxide and nitrous oxide. *Science*, *274*(5291), 1340–1343.
- 719 Butchart, N., Cionni, I., Eyring, V., Shepherd, T., Waugh, D., Akiyoshi, H., ...  
 720 others (2010). Chemistry–climate model simulations of twenty-first century  
 721 stratospheric climate and circulation changes. *Journal of Climate*, *23*(20),  
 722 5349–5374.
- 723 Chiodo, G., & Polvani, L. M. (2019). The response of the ozone layer to quadru-  
 724 pled CO2 concentrations: Implications for climate. *Journal of Climate*, *32*(22),  
 725 7629–7642.
- 726 Chou, M.-D. (1990). Parameterizations for the absorption of solar radiation by O2  
 727 and CO2 with application to climate studies. *Journal of Climate*, *3*(2), 209–  
 728 217.
- 729 Chou, M.-D. (1992). A solar radiation model for use in climate studies. *Journal of*  
 730 *Atmospheric Sciences*, *49*(9), 762–772.
- 731 Chou, M.-D., & Suarez, M. J. (1994). An efficient thermal infrared radiation param-  
 732 eterization for use in general circulation models.
- 733 Collow, A. B. M., Mahanama, S. P., Bosilovich, M. G., Koster, R. D., & Schubert,  
 734 S. D. (2017). *An evaluation of teleconnections over the united states in an*  
 735 *ensemble of AMIP simulations with the MERRA-2 configuration of the GEOS*  
 736 *atmospheric model* (Tech. Rep.).
- 737 Davis, N. A., Callaghan, P., Simpson, I. R., & Tilmes, S. (2022). Specified dynamics

- 738 scheme impacts on wave-mean flow dynamics, convection, and tracer transport  
 739 in CESM2 (WACCM6). *Atmospheric Chemistry and Physics*, 22(1), 197–214.
- 740 Dietmüller, S., Eichinger, R., Garny, H., Birner, T., Boenisch, H., Pitari, G., ...  
 741 others (2018). Quantifying the effect of mixing on the mean age of air in  
 742 CCMVal-2 and CCM1-1 models. *Atmospheric Chemistry and Physics*, 18(9),  
 743 6699–6720.
- 744 Eichinger, R., Garny, H., Šácha, P., Danker, J., Dietmüller, S., & Oberländer-Hayn,  
 745 S. (2020). Effects of missing gravity waves on stratospheric dynamics: Part 1,  
 746 Climatology. *Climate Dynamics*, 54(5), 3165–3183.
- 747 Eluszkiewicz, J., Hemler, R. S., Mahlman, J. D., Bruhwiler, L., & Takacs, L. L.  
 748 (2000). Sensitivity of age-of-air calculations to the choice of advection scheme.  
 749 *Journal of the Atmospheric Sciences*, 57(19), 3185–3201.
- 750 Eyring, V., Lamarque, J.-F., Hess, P., Arfeuille, F., Bowman, K., Chipperfield,  
 751 M. P., ... others (2013). Overview of IGAC/SPARC Chemistry-Climate  
 752 Model Initiative (CCMI) community simulations in support of upcoming ozone  
 753 and climate assessments. *SPARC Newsletter*, 40(January), 48–66.
- 754 Freitas, S. R., Grell, G. A., Molod, A., Thompson, M. A., Putman, W. M., Santos e  
 755 Silva, C. M., & Souza, E. P. (2018). Assessing the Grell-Freitas convection  
 756 parameterization in the NASA GEOS modeling system. *Journal of Advances  
 757 in Modeling Earth Systems*, 10(6), 1266–1289.
- 758 Gelaro, R., McCarty, W., Suárez, M. J., Todling, R., Molod, A., Takacs, L., ...  
 759 others (2017). The modern-era retrospective analysis for research and applica-  
 760 tions, version 2 (MERRA-2). *Journal of Climate*, 30(14), 5419–5454.
- 761 Grell, G. A., & Freitas, S. R. (2014). A scale and aerosol aware stochastic convective  
 762 parameterization for weather and air quality modeling. *Atmospheric Chemistry  
 763 and Physics*, 14(10), 5233–5250.
- 764 Groö, J.-U., & Russell III, J. M. (2005). A stratospheric climatology for O<sub>3</sub>, H<sub>2</sub>O,  
 765 CH<sub>4</sub>, NO<sub>x</sub>, HCl and HF derived from HALOE measurements. *Atmospheric  
 766 Chemistry and Physics*, 5(10), 2797–2807.
- 767 Gupta, A., Gerber, E. P., & Lauritzen, P. H. (2020). Numerical impacts on tracer  
 768 transport: A proposed intercomparison test of Atmospheric General Circula-  
 769 tion Models. *Quarterly Journal of the Royal Meteorological Society*, 146(733),  
 770 3937–3964.
- 771 Hall, T. M., & Plumb, R. A. (1994). Age as a diagnostic of stratospheric transport.  
 772 *Journal of Geophysical Research: Atmospheres*, 99(D1), 1059–1070.
- 773 Hall, T. M., Waugh, D. W., Boering, K. A., & Plumb, R. A. (1999). Evaluation  
 774 of transport in stratospheric models. *Journal of Geophysical Research: Atmo-  
 775 spheres*, 104(D15), 18815–18839.
- 776 Hardiman, S. C., Butchart, N., & Calvo, N. (2014). The morphology of the Brewer-  
 777 Dobson circulation and its response to climate change in CMIP5 simulations.  
 778 *Quarterly Journal of the Royal Meteorological Society*, 140(683), 1958–1965.
- 779 Haynes, P., McIntyre, M., Shepherd, T., Marks, C., & Shine, K. P. (1991). On the  
 780 “downward control” of extratropical diabatic circulations by eddy-induced  
 781 mean zonal forces. *Journal of the Atmospheric Sciences*, 48(4), 651–678.
- 782 Hegglin, M. I., Brunner, D., Peter, T., Hoor, P., Fischer, H., Staehelin, J., ... Weers,  
 783 U. (2006). Measurements of NO, NO<sub>y</sub>, N<sub>2</sub>O, and O<sub>3</sub> during SPURT: implica-  
 784 tions for transport and chemistry in the lowermost stratosphere. *Atmospheric  
 785 Chemistry and Physics*, 6(5), 1331–1350.
- 786 Holton, J. R., Haynes, P. H., McIntyre, M. E., Douglass, A. R., Rood, R. B., & Pfis-  
 787 ter, L. (1995). Stratosphere-troposphere exchange. *Reviews of Geophysics*,  
 788 33(4), 403–439.
- 789 Holzer, M., & Hall, T. M. (2000). Transit-time and tracer-age distributions in geo-  
 790 physical flows. *Journal of the atmospheric sciences*, 57(21), 3539–3558.
- 791 Iacono, M. J., Delamere, J. S., Mlawer, E. J., Shephard, M. W., Clough, S. A., &  
 792 Collins, W. D. (2008). Radiative forcing by long-lived greenhouse gases: Cal-

- culations with the AER radiative transfer models. *Journal of Geophysical Research: Atmospheres*, 113(D13).
- Ivy, D. J., Solomon, S., Calvo, N., & Thompson, D. W. (2017). Observed connections of arctic stratospheric ozone extremes to Northern Hemisphere surface climate. *Environmental Research Letters*, 12(2), 024004.
- Kouatchou, J., Molod, A., Nielsen, J., Auer, B., Putman, W., & Clune, T. (2015). *GEOS-5 chemistry transport model user's guide* (Tech. Rep.).
- Legras, B., Pissot, I., Berthet, G., & Lefevre, F. (2004). Variability of the lagrangian turbulent diffusivity in the lower stratosphere. *Atmospheric Chemistry and Physics Discussions*, 4(6), 8285–8325.
- Lin, S.-J. (2004). A “vertically lagrangian” finite-volume dynamical core for global models. *Monthly Weather Review*, 132(10), 2293–2307.
- Lin, S.-J., Putman, W., & Harris, L. (2017). *The gfdl finite-volume cubed-sphere dynamical core*. NWS/NCEP/EMC.
- Molod, A., Takacs, L., Suarez, M., & Bacmeister, J. (2015). Development of the GEOS-5 atmospheric general circulation model: Evolution from MERRA to MERRA2. *Geoscientific Model Development*, 8(5), 1339–1356.
- Monge-Sanz, B., Chipperfield, M., Simmons, A., & Uppala, S. (2007). Mean age of air and transport in a CTM: Comparison of different ECMWF analyses. *Geophysical Research Letters*, 34(4).
- Monge-Sanz, B. M., Bozzo, A., Byrne, N., Chipperfield, M. P., Diamantakis, M., Flemming, J., ... others (2022). A stratospheric prognostic ozone for seamless Earth system models: performance, impacts and future. *Atmospheric Chemistry and Physics*, 22(7), 4277–4302.
- Morgenstern, O., & Carver, G. D. (2001). Comparison of cross-tropopause transport and ozone in the upper troposphere and lower stratosphere region. *Journal of Geophysical Research: Atmospheres*, 106(D10), 10205–10221.
- Neu, J., Strahan, S., Braesicke, P., Douglass, A., Huck, P., Oman, L., ... Tegtmeier, S. (2010). SPARC CCMVal (2010), SPARC Report on the Evaluation of Chemistry-Climate Models: Chapter 5: Transport. SPARC.
- Neu, J. L., & Plumb, R. A. (1999). Age of air in a “leaky pipe” model of stratospheric transport. *Journal of Geophysical Research: Atmospheres*, 104(D16), 19243–19255.
- Oehrlein, J., Chiodo, G., & Polvani, L. M. (2020). The effect of interactive ozone chemistry on weak and strong stratospheric polar vortex events. *Atmospheric Chemistry and Physics*, 20(17), 10531–10544.
- Orbe, C., Oman, L. D., Strahan, S. E., Waugh, D. W., Pawson, S., Takacs, L. L., & Molod, A. M. (2017). Large-scale atmospheric transport in GEOS replay simulations. *Journal of Advances in Modeling Earth Systems*, 9(7), 2545–2560.
- Orbe, C., Rind, D., Jonas, J., Nazarenko, L., Faluvegi, G., Murray, L. T., ... others (2020). GISS Model E2.2: A climate model optimized for the middle atmosphere—2. Validation of large-scale transport and evaluation of climate response. *Journal of Geophysical Research: Atmospheres*, 125(24), e2020JD033151.
- Orbe, C., Yang, H., Waugh, D. W., Zeng, G., Morgenstern, O., Kinnison, D. E., ... others (2018). Large-scale tropospheric transport in the Chemistry–Climate Model Initiative (CCMI) simulations. *Atmospheric Chemistry and Physics*, 18(10), 7217–7235.
- Pan, L. L., Wei, J., Kinnison, D., Garcia, R., Wuebbles, D., & Brasseur, G. P. (2007). A set of diagnostics for evaluating chemistry-climate models in the extratropical tropopause region. *Journal of Geophysical Research: Atmospheres*, 112(D9).
- Pawson, S., Stajner, I., Kawa, S. R., Hayashi, H., Tan, W.-W., Nielsen, J. E., ... Livesey, N. J. (2007). Stratospheric transport using 6-h-averaged winds from a data assimilation system. *Journal of Geophysical Research: Atmospheres*,

- 848 112(D23).
- 849 Plumb, R. A. (1985). On the three-dimensional propagation of stationary waves.  
850 *Journal of Atmospheric Sciences*, 42(3), 217–229.
- 851 Plumb, R. A. (1996). A “tropical pipe” model of stratospheric transport. *Journal of*  
852 *Geophysical Research: Atmospheres*, 101(D2), 3957–3972.
- 853 Plumb, R. A. (2002). Stratospheric transport. *Journal of the Meteorological Society*  
854 *of Japan. Ser. II*, 80(4B), 793–809.
- 855 Polvani, L. M., Waugh, D. W., Correa, G. J., & Son, S.-W. (2011). Stratospheric  
856 ozone depletion: The main driver of twentieth-century atmospheric circulation  
857 changes in the southern hemisphere. *Journal of Climate*, 24(3), 795–812.
- 858 Prather, M. J., Zhu, X., Tang, Q., Hsu, J., & Neu, J. L. (2011). An atmospheric  
859 chemist in search of the tropopause. *Journal of Geophysical Research: Atmo-*  
860 *spheres*, 116(D4).
- 861 Rood, R. B. (1987). Numerical advection algorithms and their role in atmospheric  
862 transport and chemistry models. *Reviews of geophysics*, 25(1), 71–100.
- 863 Rosenlof, K. H. (1995). Seasonal cycle of the residual mean meridional circulation  
864 in the stratosphere. *Journal of Geophysical Research: Atmospheres*, 100(D3),  
865 5173–5191.
- 866 Son, S.-W., Tandon, N. F., Polvani, L. M., & Waugh, D. W. (2009). Ozone hole and  
867 Southern Hemisphere climate change. *Geophysical Research Letters*, 36(15).
- 868 Strahan, S., Douglass, A., & Newman, P. (2013). The contributions of chemistry  
869 and transport to low arctic ozone in March 2011 derived from aura MLS obser-  
870 vations. *Journal of Geophysical Research: Atmospheres*, 118(3), 1563–1576.
- 871 Thiele, G., & Sarmiento, J. (1990). Tracer dating and ocean ventilation. *Journal of*  
872 *Geophysical Research: Oceans*, 95(C6), 9377–9391.
- 873 Waugh, D., & Hall, T. (2002). Age of stratospheric air: Theory, observations, and  
874 models. *Reviews of Geophysics*, 40(4), 1–1.
- 875 Weaver, C. J., Douglass, A. R., & Rood, R. B. (1993). Thermodynamic balance  
876 of three-dimensional stratospheric winds derived from a data assimilation  
877 procedure. *Journal of Atmospheric Sciences*, 50(17), 2987–2993.